Spin and Carrier Relaxation Dynamics in InAsP Ternary Alloys, the Spin-orbit-split Hole Bands in Ferromagnetic InMnSb and InMnAs, and Reflectrometry Measurements of Valent Doped Barium Titanate

Michael A. Meeker

Dissertation submitted to the Faculty of the
Virginia Polytechnic Institute and State University
in partial fulfillment of the requirements for the degree of

Doctor of Philosophy
in
Physics

Giti A. Khodaparast, Chair
Vinh Q. Nguyen
Hans D. Robinson
Vito W. Scarola

12/02/16

Department of Physics, Virginia Polytechnic Institute and State University Blacksburg, Virginia

Keywords: Spin relaxation, III-V semiconductors, Carrier relaxation times, Phonons, Hot carriers, Magnetic semiconductors, Magneto-optical effects, Ferroelectric, Lead-free Materials, Barium Titanate

Spin and Carrier Relaxation Dynamics in InAsP Ternary Alloys, the Spin-orbit-split Hole Bands in Ferromagnetic InMnSb and InMnAs, and Reflectrometry Measurements of Valent Doped Barium Titanate

Michael A. Meeker

ABSTRACT

This dissertation focuses on projects where optical techniques were employed to characterize novel materials, developing concepts toward next generation of devices. The materials that I studied included InAsP, InMnSb and InMnAs, and BT-BCN. I have employed several advanced time resolved and magneto-optical techniques to explore unexplored properties of these structures.

The first class of the materials were the ternary alloys InAsP. The electron g-factor of InAsP can be tuned, even allowing for g=0, making InAsP an ideal candidate for quantum communication devices. Furthermore, InAsP shows promises for opto-electronics and spintronics, where the development of devices requires extensive knowledge of carrier and spin dynamics. Thus, I have performed time and polarization resolved pump-probe spectroscopy on InAsP with various compositions. The carrier and spin relaxation time in these structures were observed and demonstrated tunability to the excitation wavelengths, composition and temperature. The sensitivity to these parameters provide several avenues to control carrier and spin dynamics in InAsP alloys.

The second project focused on the ferromagnetic narrow gap semiconductors InMnAs and InMnSb. The incorporation of Mn can lead to ferromagnetic behavior of InMnAs and InMnSb, and enhance the g-factors, making them ideal candidates for spintronics devices. When grown using Molecular Beam Epitaxy (MBE), the Curie temperature (T_c) of these structures is <100 K, however structures grown using Metalorganic Vapor phase Epitaxy (MOVPE) have T_c >300 K. Magnetic circular dichroism was performed on MOVPE grown

InMnAs and InMnSb. Comparison of the experimental results with the theoretical calculations provides a direct method to map the band structure, including the temperature dependence of the spin-orbit split-off band to conduction band transition and g-factors, as well as the estimated sp-d electron/hole coupling parameters.

My final project was on the lead-free ferroelectric BT-BCN. Ferroelectric materials are being investigated for high speed, density, nonvolatile and energy efficient memory devices; however, commercial ferroelectric memories typically contain lead, and use a destructive reading method. Reflectometry measurements were used in order to determine the refractive index of BT-BCN with varying thicknesses, which can provide a means to nondestructively read ferroelectric memory through optical methods.

Spin and Carrier Relaxation Dynamics in InAsP Ternary Alloys, the Spin-orbit-split Hole Bands in Ferromagnetic InMnSb and InMnAs, and Reflectrometry Measurements of Valent Doped Barium Titanate

Michael A. Meeker

GENERAL AUDIENCE ABSTRACT

This dissertation focuses on the characterization of materials that are important for the next generation computer architecture through optical techniques. These materials include the ternary alloy InAsP, the ferromagnetic semiconductors InMnAs and InMnSb, and the lead-free ferroelectric BT-BCN.

InAsP is a ternary alloy composed of the technologically important InAs and InP, and by changing the alloy composition, the band gap and g-factor can be tuned. This allows for InAsP to have band gaps within the communication band, which is important for fiber optic communications as well as infrared photodetectors. As the functionality of these devices depends on the carrier dynamics, I have performed pump-probe spectroscopy in order to probe the carrier and spin relaxation times of this material system. These relaxation times were found to vary with excitation wavelengths, allowing flexibility in the application of this material system for devices.

InAs and InSb are attractive materials for device applications because they offer large electron g-factor, small effective masses, and high mobilities. With the incorporation of Mn, these materials can become ferromagnetic, allowing for their use in ferromagnetic memories as well as other possible devices. The theory of ferromagnetism in semiconductors relies on the interaction between the itinerant holes and the Mn ions, however, in narrow gap semiconductors there is a large band mixing between the conduction and valence band states, and thus the interaction between the conduction band electrons and the Mn is important. In this study, my measurements revealed several interband transitions, which allowed for the

calculation of the coupling constants between the electrons, holes and the Mn.

My final study involved the lead-free ferroelectric BT-BCN. Ferroelectric materials are ideal for fast, low power and nonvolatile memories; however, typical implementation utilizes materials that contain lead, and a destructive reading mechanism, requiring a rewrite step. Optical, nondestructive reading methods are being explored based off of the rotation of the polarization of light as it passes through the sample. As this requires knowledge of the refractive index, I performed reflectometry measurements in order to determine the refractive indices of several BT-BCN films.

GRANT INFORMATION

The experiments performed in chapter 2 was supported by the NSF-Career Award DMR-0846834, and by the National High Magnetic Field Laboratory through a UCGP. The work in chapter 3 was supported by the AFOSR through Grant FA9550-14-1-0376. In addition, Giti Khodaparast, Brenden Magill, and Michael Meeker were supported by NSF-Career Award DMR-0846834 and Bruce Wessels was supported by NSF-DMR-60035274 and NSF-DMR-1305666. Steve McGill acknowledges support from the NSF MRI program (DMR-1229217). A portion of this work was performed at the National High Magnetic Field Laboratory, which is supported by National Science Foundation Cooperative Agreement No. DMR-1157490 and the State of Florida. The measurements in chapter 4 were supported by the AFOSR through grant FA9550-14-1-0376.

Acknowledgments

Dr. Giti Khodaparast, for taking me as her student, allowing me the opportunities to travel to national laboratories, the ability to collaborate with other research groups, as well as offering assistance, advice and encouragement.

Dr. Brenden Magill, for assisting me with various projects, and offering advice and encouragement.

Dr. Travis Merritt and Dr. Mithun Bhowmick, for teaching me how to perform the various experiments.

Dr. Steve McGill, for helping me perform experiments in the National High Magnetic Field Laboratory, as well as being around at inconvenient times when we ran into issues.

Dr. Joseph Tischler, for inviting me to the Naval Research Laboratory in order to perform measurements, where I learned new techniques during the visit.

Dr. Mantu Hudait and Michael Clavel, Dr. Chris Stanton and Dr. Dipta Saha, for their collaborations and discussions on a variety of projects, I learned topics beyond traditional physics training that would be important for my future career.

Betty Wilkins, for helping to guide me through the requirements for graduate students.

Rathsara Herath, and Alejandro Sosa, for their assistance in performing various experiments.

My family, for all of their assistance and encouragement over the years.

Attributions

Chapter 2: Authorship is shared equally with Brenden Magill. The structures were grown by Sukgeun Choi, who was supervised by Chris Palmstrøm. Kelly McCutcheon assisted the creation of the set up, with advice from Mithun Bhowmick. The time resolved photoluminescence data was taken by Travis Merritt with the assistance of Steve McGill. Giti Khodaparast supervised the project.

Chapter 3: Authorship is shared equally with Brenden Magill. Steve McGill assisted with the experimental set up, while theoretical calculations were performed by Dipta Saha under the supervision of Chris Stanton. The structures were grown by Bruce Wessels and the project was supervised by Giti Khodaparast.

Contents

List of Figures

List of Tables

Chapter 1

Introduction

1.1 Summary

In order to develop this dissertation, several advanced optical and magneto-optical techniques were utilized to study material systems important for next generation computer architecture, spintronic devices, and infrared sensors. These materials include: InAsP, which shows promise for quantum communication devices due to the ability to achieve g=0, the ferromagnetic semiconductors InMnAs and InMnSb, allowing for the creation of novel multifunctional devices utilizing the spin and charge, and the ferroelectric (1-x) $BaTiO_3$ (BTO)-xBa($Cu_{1/3}Nb_{2/3}$)O_3 (BT-BCN), x=0.025, a candidate for lead-free ferroelectric based memories. In this section, I introduce these material systems and present an introduction to the other chapters of this dissertation. This chapter also provides an overview of experimental techniques used in this study, the additional projects in which I was involved, and the nature of my collaborations. Chapter 5 reviews the results of these studies, and presents ideas for future projects.

Chapter 2 discusses my time and polarization-resolved differential transmission measurements on InAsP. InAsP ternary alloys are attractive materials for a variety of optoelectronic applications, including modern and improved optical telecommunication [1, 2], broadband photodetectors [3] and mid-IR lasers [4, 5, 6]. In addition, InAsP can offer a wide range of g-factors; including g=0, a desired characteristic for semiconductor-based quantum communication applications [7, 52]. For quantum communication applications, it is important that in the conduction band, both spin split levels absorb equally of the exciting photons, while the spin split states in the valance band should be resolved [8]. Therefore, materials in which the g-factor of the conduction band is much smaller than the g-factor of the valence band hole would be important and in this direction InAsP [1, 5, 7] could be an ideal candidate.

Chapter 3 presents my study on the magnetic circular dichroism (MCD) of the ferromagnetic semiconductors InMnAs and InMnSb. Compound semiconductors such as InAs and InSb have unique properties that result from their narrow band gap, including small effective masses, high electron mobilities and large g-factors. There is a rapidly growing interest in the science and engineering of multifunctional narrow gap semiconductors that include magnetic elements, such as Mn, which can lead to ferromagnetism [9], giant magnetoresistance, and even enhanced g-factors. As a result, structures based on these materials have potential to lead novel and revolutionary devices such as spin transistors [10], spin-LEDs/lasers, infrared spin-photonics, ultrafast switches [11] and spin logic circuits [12]. Progress in this important area has been aided by the development of metalorganic vapor phase epitaxy (MOVPE) growth techniques, where InMnAs and InMnSb alloy films have been grown with Curie temperatures *(T_c)* above room temperature [13, 14, 15, 16, 17].

The first III-V ferromagnetic semiconductor alloy, $In_{1-x}Mn_xAs$, was prepared by molecular beam epitaxy (MBE) with a T_c of the order of $\sim$50 K [18]. Subsequent studies demonstrated T_c closer to 90 K [78]. Low temperature MBE was nearly exclusively used to prepare

InMnAs thin films, although MOVPE, an alternate technique, demonstrated that single phase magnetic InMnAs compounds could be deposited at 500 ^{o}C, 200 ^{o}C higher than that used in MBE. Furthermore, InMnAs films deposited using MOVPE demonstrate ferromagnetism with a T_c of 330 K [13, 14, 15, 16]. Most of the current research activities in the area of ferromagnetic semiconductors have been focused on III-Mn-V alloys such as GaMnAs [19, 20, 21, 22, 23, 24] with small lattice constants and large valence band effective masses; therefore it is important in this context to explore the opposite extremes of the III-Mn-V ternaries, *i.e.*, InMnAs and InMnSb with larger spin-orbit couplings. In addition, due to a smaller hole effective mass and higher hole mobility, carrier transport in InMnAs and InMnSb would be enhanced compared to the other III-V ferromagnetic structures such as GaMnAs.

My study of the ferroelectric (FE) (1-x) $BaTiO_3$ (BTO)-xBa$(Cu_{1/3}Nb_{2/3})O_3$ (BT-BCN) is discussed in Chapter 4. FE materials are of considerable interest for memory applications due to their low power consumption [25, 96], fast speeds [95, 96], and high memory density [26]. Current implementation of FE based memory devices typically contain lead, and the memory is read in a destructive manner [96]. In order to combat these issues, improved lead-free FE are being developed, and new processes for reading the memory are being explored. Nondestructive reading of FE memory can be performed with optical methods, for example, by utilizing the Pockels effect [101, 102], where the application of an electric field changes the refractive index. In this scheme, light with polarization that is not parallel to the optical axises transmits through the FE, causing a rotation of the polarization angle, dependent on the direction of the electric dipole moment. When the transmitted light is incident on a polarizer, the intensity of the light will differ depending on the degree of rotation, allowing for the state of the FE to be determined optically. BTO is a lead-free FE, and was found to have large Pockels coefficients [101, 102], and when doped with Ba$(Cu_{1/3}Nb_{2/3})O_3$, the

longitudinal piezoelectric response and electromechanical coupling constant were found to increase [99]. Thus, BT-BCN has the potential to be used as optically read FE memory.

1.2 Experimental Techniques

The projects that are focused on in this dissertation utilized a wide variety of optical techniques, in order to probe carrier dynamics, band structures, and refractive indices. The techniques of time and polarization-resolved pump-probe spectroscopy, MCD, and reflectometry, were performed in chapters 2, 3, and 4 respectively, and a description for how these experiments were performed is provided in this section. Aside from the experiments described here, I have also performed photoluminescence, piezoluminescence, and Hall effect measurements.

In chapter 2, time and polarization resolved differential transmission pump-probe spectroscopy were performed on InAsP ternary alloys in order to study the carrier and spin dynamics in this material system. In pump-probe spectroscopy, light from pulse lasers are separated into two paths with a variable path length difference. One of the paths, referred to as the pump, excites the carriers, changing the absorption coefficient of the material. The alternate path is used in order to probe the change in absorption by measuring the intensity of light that is either reflected or transmitted through the sample, and hence is called the probe. The intensity of the light in the pump:probe for my experiments was $\sim$1000:1, ensuring that the absorption of the probe caused negligible changes to the dynamics. The time delay between the pump and probe was controlled via retroreflector on a movable stage. Furthermore, the pump and probe paths can be polarized with either the same (SCP), or opposite (OCP) circular polarization. Due to the conservation of angular momentum, the absorption of circularly polarized light changes the spin state of electrons by ± 1, with the

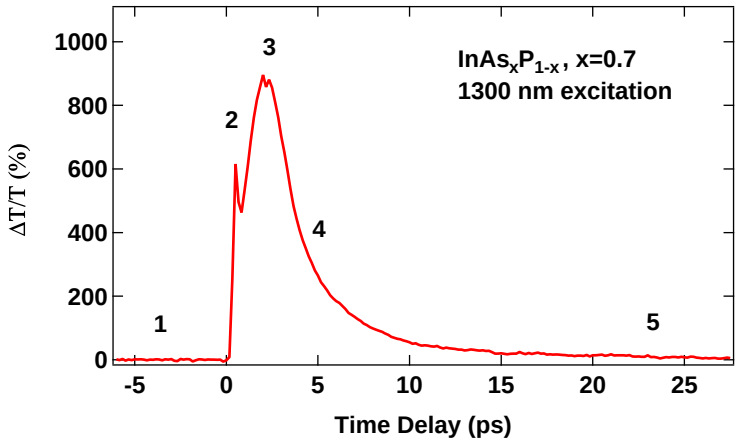

Figure 1.1: An example of my pump-probe results of $InAs_xP_{1-x}$, x=0.7, and the pump and probe have a wavelength of 1300 nm. There are five main features depicted. Region 1, the probe arrives at the sample before the pump, and is taken to be the background transmission. Region 2, the pump and probe arrive at the same time, resulting in changes to the transmission of the sample. Region 3, the probe pulse arrives at the sample after the pump pulse. The pump excites a large number of carriers to the conduction band, where effects such as band filling and band gap renormalization change the absorption coefficients. Region 4, carrier recombination starts, reducing the effects of band filling and band gap renormalization, and after long times, region 5, the transmission completely returns to the background level.

+1 (-1) being for the absorption of right (left) handed circularly polarized light. Therefore, the transmission through the sample for the SCP and OCP configuration differs, and the difference can be used in order to determine the spin relaxation time. An example of my time resolved differential transmission measurements can be seen in Fig. 1.1.

Chapter 3 discusses my study on the MCD of the ferromagnetic InMnAs and InMnSb. MCD is a measure of the difference in the absorption between left (LCP) and right (RCP) handed circularly polarized light. Due to the conservation of angular momentum, circularly polarized light changes the angular momentum by 1, and depiction of possible transitions resulting from LCP and RCP circularly polarized light can be seen in Fig. 1.2. The degeneracy of the spin states is lifted by the application of a magnetic field, changing the

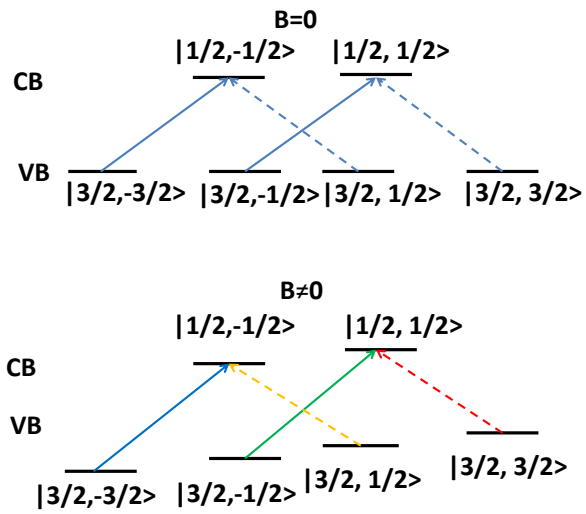

Figure 1.2: Top: A simplified picture of the conduction band (CB) and valence band states (VB), neglecting the spin-orbit split-off band, at k=0 and no external magnetic field. Due to angular conservation, LCP changes the spin state by -1, dashed lines, while RCP changes the spin state by 1, solid lines. Bottom: An external magnetic field is applied, lifting the degeneracy the the spin states. The absorption of LCP for the $|3/2, 3/2\rangle$ to $|1/2, 1/2\rangle$ transition occurs at lower energies than the RCP induced $|3/2, -3/2\rangle$ to $|1/2, -1/2\rangle$ transition.

absorption edge for LCP and RCP light. As seen in Fig. 1.2, without a magnetic field, the material can absorb LCP and RCP light equally, however, when a magnetic field is applied, the absorption edge changes for left and right handed circular polarization. In this example, the $|3/2, 3/2\rangle$ heavy hole state can be excited to the $|1/2, 1/2\rangle$ conduction band state by the absorption of LCP at lower energies than the $|3/2, -3/2\rangle$ can transition to the $|1/2,-1/2\rangle$ by the absorption of RCP, resulting in a large MCD signal at energies corresponding to the $|3/2, 3/2\rangle$ to $|1/2, 1/2\rangle$ transition. Furthermore, the application of the magnetic field changes the density of states of a bulk material to a 1D density of states, which decreases with energy. In my experiments, I averaged the MCD signal taken at positive and negative fields in order to remove any signal not originating from the sample.

Chapter 4 presents my reflectometry studies on BT-BCN. In my study, reflectometry

measures the polarization of light after reflecting off of the sample surface. The polarization of light can be decomposed into s and p-polarized states, with the s (p)-polarization being perpendicular (parallel) to the plane of incidence. Due to differing boundary conditions for light with polarization parallel and perpendicular to the surface of the material, the reflection coefficient for s and p-polarized light differs, causing a rotation of the polarization angle. In my measurements, the polarization of the reflected light was determined by varying an analyzer, consisting of a linear polarizer. The incident polarization of light was varied using a Glan-cube, varying the s and p components of the electrical field. This allowed for the determination of the ratio of reflection coefficients for s and p-polarized waves, and the refractive index was determined through the application of the Fresnel equations.

1.3 Contributions to other works

Aside from the works presented here, I have performed various luminescence measurements, primarily photoluminescence (PL), on various material systems. As of this writing, two have been published, one has been submitted, and two are being developed for submissions.

1.3.1 The Photoluminescence of InAsP

Ternary alloys are susceptible to nonuniform composition, referred to as alloy disorder, which can decrease device performance and alters carrier dynamics. In order to determine the degree of which alloy disorder is present in $InAs_xP_{1-x}$, with x=0.13 and x=0.4, magneto-PL was performed at various temperatures and magnetic fields. Through the use of lineshape analysis, the effects of the applied magnetic field on the line widths, and the temperature

dependence of the peak position, it was concluded that the x=0.13 composition was mostly devoid of alloy disorder, however alloy disorder played an important role in the PL of the x=0.4 composition. My involvement consisted of assisting with the creation of the set up and data collection.

Publication: T. R. Merritt, **M. A. Meeker**, B. A. Magill, G. A. Khodaparast, S. McGill, J. G. Tischler, S. G. Choi and C. J. Palmstrøm, J. Appl. Phys. 115, 193593 (2014)

1.3.2 The Photoluminescence of InAs/GaSb

Tunnel field-effect transistors can be employed for a wide variety of device applications ranging from energy-efficient transistors [27, 28], to quantum cascade lasers [29, 83], and solar cells [30, 31]. While the highest tunnel current in these transistors were exhibited by InAs/GaSb [32], the development of these heterojunctions is hampered due to the difficulty in creating a high quality interface between the InAs and the GaSb layers. This interface can either be InSb-like or GaAs-like, with the latter introducing lattice mismatch defects [33]. This study focused on the growth of high quality InAs/GaSb on GaAs, where my involvement pertained to the PL measurements of this structure. The PL taken in this heterojunction exhibited no signs of radiative defects, and the observable PL from the GaSb layers at room temperature, shown in Fig. 1.3 is a testament to the high quality of the structure.

Publication: J-S. Liu, M. B. Clavel, R. Pandey, S. Datta, **M. A. Meeker**, G. A. Khodaparast, and M. K. Hudait, J. Appl. Phys. 119, 244308 (2016)

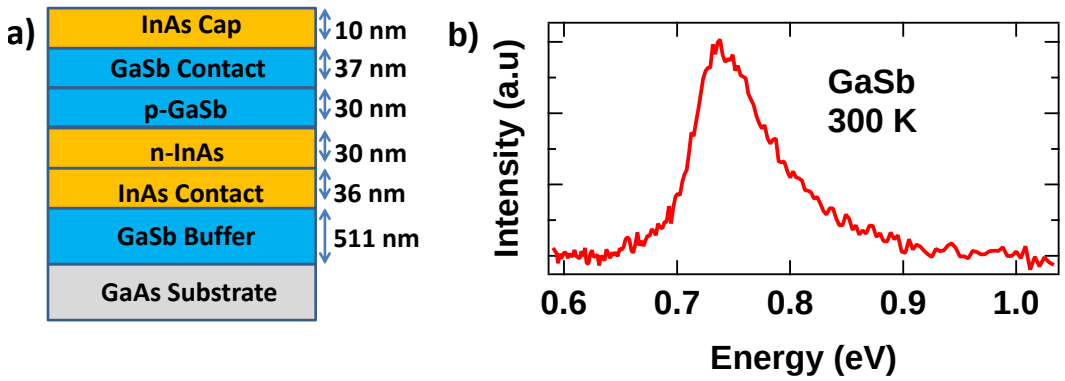

Figure 1.3: a) The layer structure of the InAs/GaSb material under investigation. The photoluminescence in b), is attributed to band to band transitions in GaSb.

1.3.3 The Photoluminescence of GaAsSb

GaAsSb is currently being investigated for potential device applications including tunneling field effect transistors [34], and infrared photodetectors [35]. However, there are several challenges to realizing these material systems, including a large miscibility gap [36], and the formation of oxides on the surface leading to surface recombination, lowering device performance [37]. The miscibility gap can be overcome by using nonequilibrium growth techniques, while surface passivation can decrease surface recombination [37]. My involvement in this study focused on the PL of several compositions of GaAsSb. The PL was used in order to find the dependence of the alloy concentration on the band gap at room temperature and 77 K, as well as to determine the quality of the samples. PL measurements were also performed on samples with differing passivation times, in order to observe its effect on the PL intensity, and thus sample quality. This work is currently being prepared for submission.

Publication: M. K. Hudait, M. Clavel, S. Saluru, J-S. Liu, M. Meeker, G. A. Khodaparast, and R. J. Bodnar, *Vibrational, Optical and Metal-Oxide-Semiconductor Characteristics of*

Sulfur Passivated GaAs1-ySby Materials with Tunable Antimony Compositions (Currently being prepared for submission)

1.3.4 The Photoluminescence of Ge

Aside from having a lower band gap than Si, Ge has higher electron and hole mobilities, useful for low-power devices [41]. Furthermore, as the direct gap is at 1550 nm, much interest has been generated for opto-electronic applications and lasers. I have performed photoluminescence measurements on n-Ge grown on Si, and AlAs/GaAs, and p-Ge grown on AlAs/GaAs. The photoluminescence was used in order to show sample quality, determine the location of the band gaps as a function of temperature and power, and to possibly identify defect states.

1.3.5 The Piezoluminescence of ZnS:Cu

Piezoluminescence (PZL) refers to the emission of light when mechanical force is applied to the material, and is an attractive candidate for uses in sensors to monitor damage accumulation in infrastructure [38], bioimaging [39], and artificial skins to detect mechanical stress [40]. As devices utilizing PZL are being developed methods for increasing the luminescence are being explored. In this study, ZnS:Cu underwent hydrogenation at various temperatures in order to facilitate the creation of S vacancies, believed to increase the PZL emission, and is then incorporated into an elastomer. In this work, I performed PZL measurements on samples that underwent hydrogenation at various temperatures; an example emission is shown in Fig. 1.4.

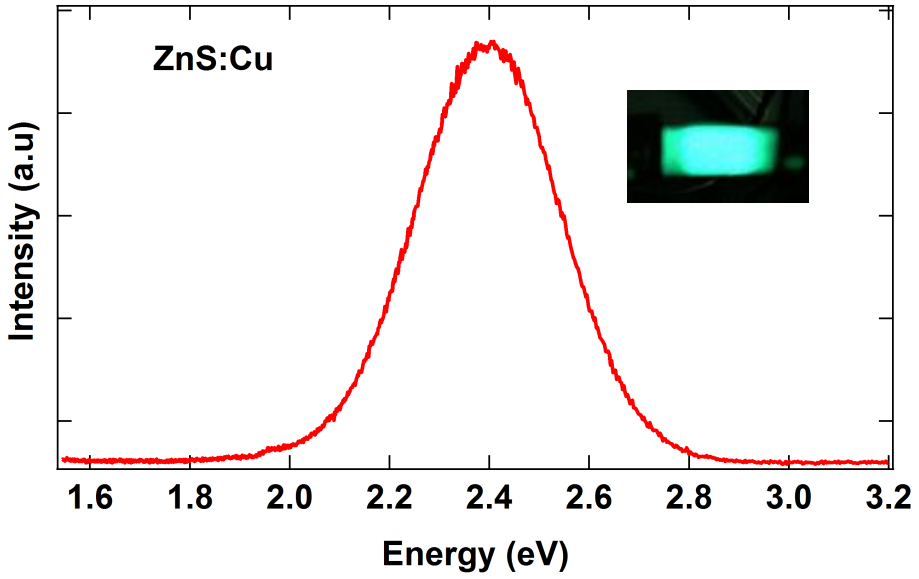

Figure 1.4: The figure shows an example PZL spectra of ZnS:Cu, while being stretched. The inset shows a picture of the structure being stretched.

Publication: J. Gan, M. G. Kang, **M. A. Meeker**, G. A. Khodaparast, R. J. Bodnar, J. E. Mahaney, D. Maurya, and S. Priya, *Enhanced piezoluminescence in defect-engineered ZnS:Cu microparticles for flexible light emitting elastomers.* (Submitted to Advanced Energy Materials)

1.4 Collaborations

This dissertation established close collaborations with several materials scientists including the groups of Profs. Bruce Wessels: Northwestern University, Chris Palmstrøm: Univ. of California Santa Barbara, Shahshank Priya (VT) and Mantu Hudait (VT) who provided the structures studied in these projects. I also worked closely with Dr. McGill at National High Magnetic Field Laboratory (NHFML) in Florida, and Dr. Joe Tischler at the Naval Research laboratory.

Several experiments in this work were performed at the NHFML. In chapter 2, the time resolved PL was taken using SCM3, a 17 T superconducting magnet, that can have cryostat temperatures between 4-300 K. Light reaches the samples in the SCM3 magnet by going through a window underneath, and light is collected using a fiber optic. All of the MCD measurements in chapter 3 were taken at the NHMFL using the Split-Florida Helix magnet, which has can reach temperatures between 15-190 K. The Split-Florida Helix magnet has large optical window on the four sides of the cryostat, allowing for the collection of light without the need for fiber optics, which allows for polarization dependent measurements. The magnet can typically reach to 25 T, although depending on the experiment and geometry, the probe can be placed in the maximum of the magnetic field at roughly 31 T, however, this would require collection though an optical fiber. Dr. McGill was instrumental in these measurements, as he has helped to load the samples, transfer helium, assisted with the experimental set up and trouble shootings.

Figure 1.5: The set up used for the MCD measurements. The Split-Florida Helix magnet has optical windows, which preserve the polarization of light, and can provide magnetic fields of upto 31 T.

Reproduced from M. A. Meeker, B. A. Magill, T. R. Merritt, M. Bhowmick, K. McCutcheon, G. A. Khodaparast, J. G. Tischler, S. McGill, S. G. Choi and C. J. Palmstrøm, Applied Physics Letters, 102, 222102 (2013), with the permission of AIP Publishing.

Chapter 2

Dynamics of photoexcited carriers and spins in InAsP ternary alloys

M. A. Meeker[1], B. A. Magil[1], T. R. Merritt, M. Bhowmick, K. McCutcheon,

G. A. Khodaparast [2]

Department of Physics, Virginia Tech, Blacksburg, VA 24061, USA

J. G. Tischler

Naval Research Laboratory, Washington, DC 20375, USA

S. McGill

National High Magnetic Field Laboratory Florida, Tallahassee, FL. 32310, USA

S. G. Choi

National Renewable Energy Laboratory, Golden, CO 80401, USA

C. J. Palmstrøm

Department of Electrical and Computer Engineering, University of California, Santa Barbara, CA 93106, USA

[1]M. A. Meeker and B. A. Magill contributed equally to this work

[2]Author to whom correspondence should be addressed. Electronic mail: khoda@vt.edu..

Abstract

The recent rapid progress in the field of spintronics involves extensive measurements of carrier and spin relaxation dynamics in III-V semiconductors. In addition, as the switching rates in devices are pushed to higher frequencies, it is important to understand carrier dynamic phenomena in semiconductors on femtosecond time-scales. In this work, we employed time and spin resolved differential transmission measurements; to probe carrier and spin relaxation times in several InAsP ternary alloys. Our results demonstrate the sensitivity of the spin and carrier dynamics in this material system to the excitation wavelengths, the As concentrations, and temperature.

2.1 Introduction

Recently, g-factor engineering [42] has attracted much attention for potential applications in spintronics and in the case of InAsP ternary alloys, a wide range of g-factors, including g=0, can be achieved. The recent rapid progress in the field of spintronics involves extensive measurements of carrier and spin relaxation dynamics in III-V semiconductors. In addition to spintronics applications, this material system is important for high-speed electronic as well as optoelectronic devices. Therefore, as the switching rates in devices are pushed to higher frequencies, it is important to understand carrier dynamic phenomena in semiconductors on femtosecond time-scales. In this work, we employed time and polarization-resolved differential transmission measurements to probe carrier and spin relaxation times in several InAsP ternary alloys.

InAsP is a ternary compound with characteristics between that of InAs and InP. The observed spin relaxation time in InP demonstrated tunability as a function of the carrier

density, frequency, and intensity [43, 44, 45], and can be on the order of tens of picoseconds at room temperature (RT) [43, 44] in bulk InP, or hundreds of microseconds in charged quantum dots [46]. Several groups probed the spin life time in InAs using pump/probe spectroscopy, finding a spin life time of 24±2 ps for nearly-degenerate epitaxial layers of n-type InAs [47] and $\sim 19 \pm 4$ ps for intrinsic material [48]. Hall *et al.* [49] studied spin relaxation in (110) and (001) InAs/GaSb heterostructures and a spin lifetime of 18 ps was reported for (110) superlattices, much longer than that of the (001) structure with a life time of 700 fs. The large enhancement has been explained by the suppression of decay associated with asymmetry in interface bonding and bulk inversion asymmetry (BIA) contributions to the spin decay process in (110) superlattices. Litvinenko *et al.* measured spin lifetime in three undoped InAs films of different thicknesses (0.15, 0.27, and 1 μm) and for temperatures ranging from 77 K to 290 K [50]. Spin lifetimes of 1 and 20 ps were observed for 0.15 μm and 1 μm thick films, respectively, with the samples at 77 K. The measured spin relaxation time, using the magneto-optical Kerr effect spectroscopy in n-type InAs demonstrated a strong dependence on the laser fluence with the time scale of the relaxation ranging from 1 to 5 ps [51]. Our results demonstrate sensitivity of the spin and carrier dynamics in $InAs_xP_{1-x}$ alloys to excitation wavelengths, As concentrations, and temperature.

In this work, $InAs_xP_{1-x}$ alloys with the compositions ranging from x=0.4 to 0.75, grown on Fe-doped semi-insulating InP(001) by chemical beam epitaxy, were studied. The thicknesses of the $InAs_xP_{1-x}$ alloys vary from 4.3 to 5.5 μm, which is larger than the critical thickness for strain relaxation [52]. Details of the growth and structural properties are described in Ref. [52]. In this study, we employed degenerate Time Resolved Differential Transmission (TRDT) pump/probe measurements where the laser source was an Optical Parametric Amplifier (OPA). The OPA itself was pumped by an amplified Ti:sapphire oscillator with a repetition rate of 1 KHz. The pump/probe pulses were tuned in the vicinity of

the band gap and ranged from 1280-1350 nm. The pulses had a duration of $\sim$ 100 fs defining the resolution of the measurements with the ratio of the pump:probe of 1000:1. Both beams were focused onto the sample with a spot size of around 150-200 μm for probe and slightly larger for the pump. The differential transmissivity, as a function of the time delay between the pump and probe pulses using an InGaAs detector, was measured.

As a result of selection rules for interband transitions, spin-polarized carriers can be created using circularly polarized pump beams. By monitoring the transmission of a weaker, delayed probe pulse that has the same circular polarization (SCP) or opposite circular polarization (OCP) as the pump pulse, the optical polarization P=(SCP-OCP)/(SCP+OCP) can be extracted. The optical polarization P decays exponentially with a decay constant related to the spin lifetime as following: $P = P_0 exp(-t/\tau_s)$, where P_0 is a constant. Examples of our TRDT and Spin Polarized Differential Transmission (SPDT) are presented here, providing information on the carrier and spin relaxation time scale in this material system.

Figure 2.1(a) shows TRDT for $InAs_{0.75}P_{0.25}$ with the pump and probe λ = 1280 - 1350 nm, with an estimated photo-excited carrier density on the order of $1 \times 10^{19} cm^{-3}$. The TRDT shows several features, including a sharp change in transmission lasting for $<$ 1 ps which can be attributed to a coherent artifact, commonly observed in a degenerate pump and probe scheme. The sharp increase is followed by a slower component which is dominated by photo-induced bleaching. Due to the *Pauli exclusion* principle, a large density of photo-excited electrons in the conduction band can reduce the amplitude of the interband optical absorption transitions via band and state filling. This leads to a decrease in the absorption, and a corresponding increase in the transmission, which is referred as photo-induced bleaching. The differential transmission can be written as: $\Delta T/T = e^{-(\alpha_0 - \alpha)L} - 1$ where T is the transmission, α_0 is the pre-excitation absorption coefficient and L is the thickness of the sample [53].

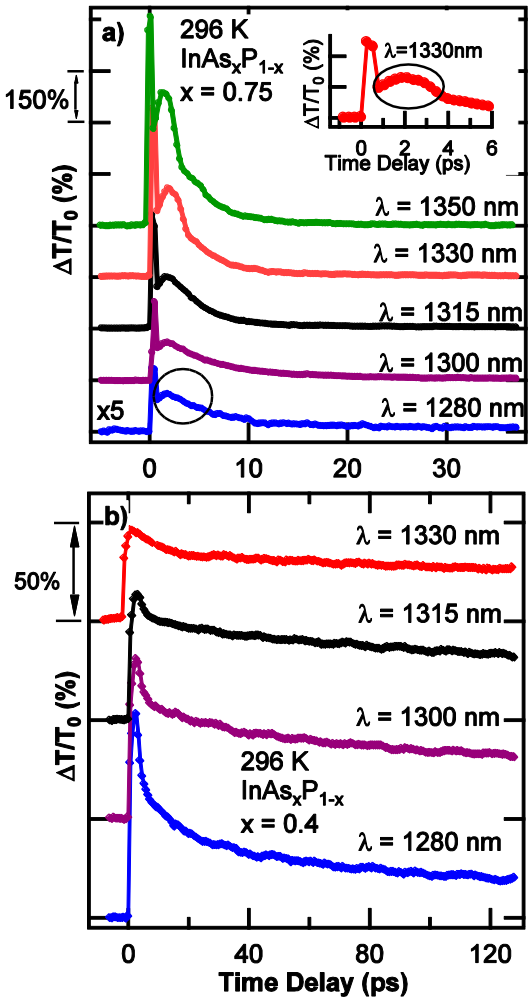

Figure 2.1: Differential transmission of (a) $InAs_{0.75}P_{0.25}$ (b) $InAs_{0.40}P_{0.60}$ for different pump and probe wavelengths; the traces are offset for clarity. The inset shows an example of the initial temporal evolution τ_1, which can be attributed to the relaxation of the hot electrons through emission of LO-phonons. The time scale, denoted by τ_1, increases by increasing the excitation, and this increase is more pronounced for the sample with x=0.75 than x=0.4, where the excitation wavelengths for pump and probe are deeper in the conduction band.

In a thick optical medium, a small change in the absorption coefficient, can accumulate to a large change in the transmission. The large photo-bleaching observed here can be expected since the sample thicknesses range from 4.3 to 5.5 μm. The relaxations of the photo-induced carriers in our samples can be modeled by two time constants, τ_1 and τ_2, where τ_1 is attributed to the initial carrier cooling and τ_2 to the relaxation time of hot electrons toward the bottom of the conduction band. The recombination time scales depend strongly on the As concentration, temperature and the excitation wavelengths. In our carrier relaxation, the initial component of the temporal evolution can be attributed to the relaxation of the hot electrons. When a hot electron gas is created at room temperature, the carrier relaxation slows down since as the electron gas cools to the lattice, the lattice temperature rises and subsequently, the number of equilibrium LO-phonons increase. In the regime of high electron densities, due to screening effects and hot phonons, the hot electrons experience a significant reduction in their energy loss rate through the emissions of LO phonons. Thus, we identify τ_1 as the thermalization time of the hot carriers which can be on the order of $\sim$2-5 ps (as shown in the inset of Fig. 2.1(a) for x=0.75 at 1330 nm), and τ_2 to the carrier relaxation time toward the bottom of conduction band, where the recombination time occurs on longer time scales depending on the As concentration and the excitation wavelength. Comparing the measurements presented in the inset of Fig. 2.1(a) at 1330 nm, for $InAs_{0.75}P_{0.25}$, to the measurements at the shorter wavelengths, we observed longer time scales for τ_1 with increasing excitation energy, where the increasing contribution of LO-phonons reduce the energy loss rate. The excitation energy dependence of τ_1 is more pronounced for the sample with a higher As concentrations where the excitation wavelengths for the pump and probe are deeper in the conduction band, compared to the measurements in Fig. 2.1(b) for $InAs_{0.4}P_{0.6}$.

In addition, as shown in Fig. 2.1(b), the carrier recombination time scale of $InAs_{0.4}P_{0.6}$ is much longer than the sample with x=0.75. Time-resolved photoluminescence (TRPL)

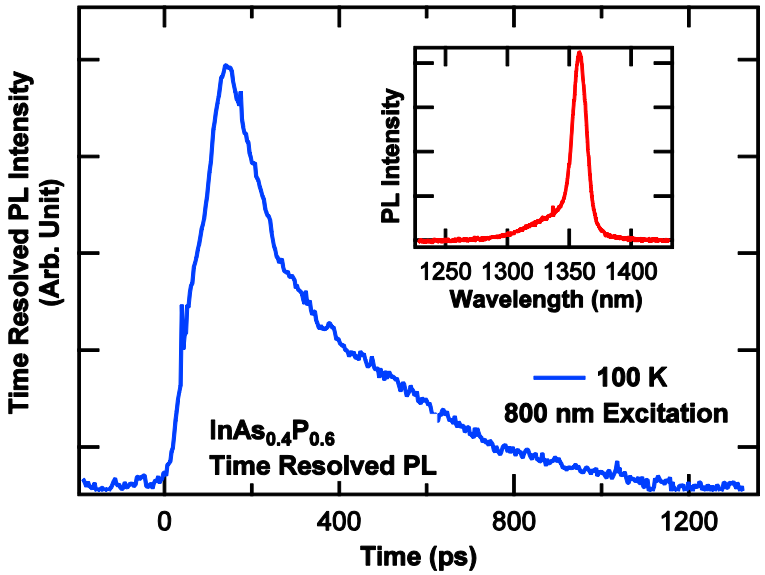

Figure 2.2: Example of time resolved PL for $InAs_{0.4}P_{0.6}$ where the PL emission in this sample, as show in the inset, was in the range detectable by a streak camera.

measurements allowed us to determine the carrier recombination time of $InAs_{0.4}P_{0.6}$, where photo-generated carrier lifetimes can be obtained by monitoring the transient PL signal after laser pulsed excitations. An example of the PL and the TRPL using a streak camera, for $InAs_{0.4}P_{0.6}$, are shown in Fig. 2.2. The excitation wavelength was fixed at 800 nm with a pulse duration of 100 fs and repetition rate of 1 KHz. The TRPL below 100 K in this sample demonstrated a recombination time on the order of $\sim$ 1.0 ns with a weak temperature dependence.

Figure 2.3 shows the time scale of the carrier relaxations τ_2, at 296 K, for the samples with different As concentrations of x = 0.4, 0.6, 0.7, and 0.75, at different excitation wavelengths. We observed that the relaxation times for the sample with x=0.4 are considerably different, ranging from 40-130 ps compared to $\sim$2-6 ps for the samples with the higher As concentrations. The long relaxation times for the sample with x = 0.4 are comparable to

the carrier relaxation times previously observed in bulk InP [43, 44]. The faster relaxation time in the sample with higher As concentrations could be related to higher defects states as well as increasing band mixing expected in the narrow gap band structures.

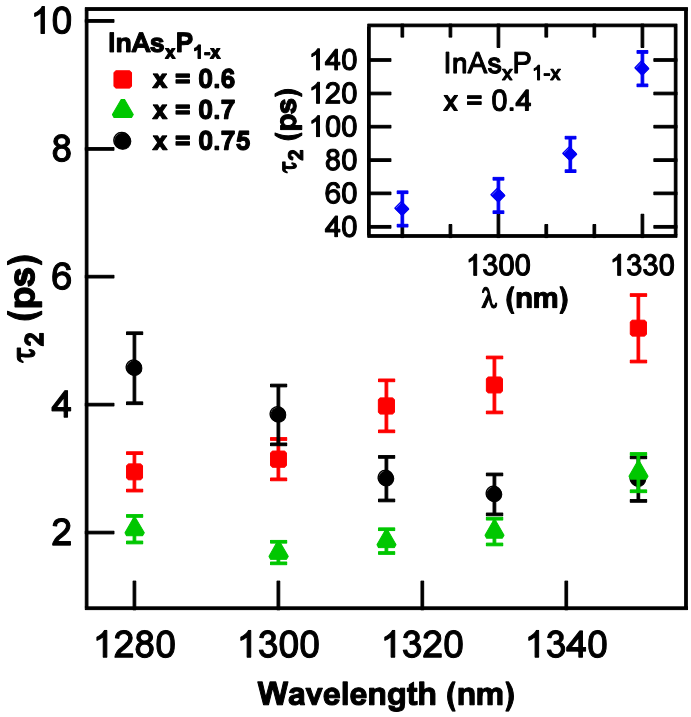

Figure 2.3: Carrier relaxation time at 296 K, τ_2, versus λ for $InAs_xP_{1-x}$ with As concentrations $x = 0.6$, 0.7, and 0.75 extracted from the exponential fits. The inset shows τ_2 for $x = 0.4$.

In order to probe the relaxation of photo-excited spin polarized carriers, two identical quarter wave plates were used to extract the SPDT for different pump/probe wavelengths. Figure 2.4 shows an example of the SPDT for $InAs_{0.75}P_{0.25}$, where the differential transmission for the pump and probe being SCP or OCP, were employed to calculate the spin relaxation time. As shown in the inset, by an exponential fit to the difference (SCP-OCP) the spin relaxation time can be extracted. The observed spin relaxation times for our sample structures are summarized in Fig. 2.5, where the longest spin relaxation was observed in

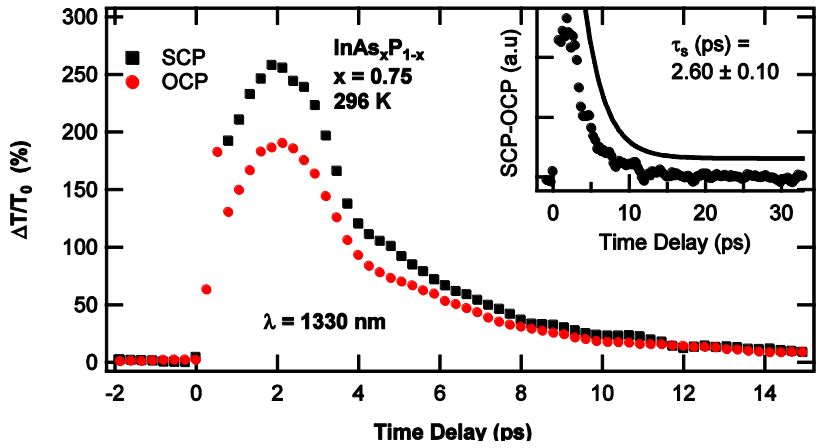

Figure 2.4: Differential transmission of $InAs_{0.75}P_{0.25}$ for $\lambda = 1330$ nm excitation. SCP denotes data taken with the pump and the probe beams having the same circular polarization while OCP denotes them having opposite circular polarizations. Inset is SCP-OCP for the traces in the graph and the spin relaxation time was extracted by fitting an exponential to the SCP-OCP. The fit is shifted for clarity.

the sample with x=0.4, ranging from 20-60 ps. The observed spin relaxation times in the samples with the As concentration larger than 0.4, are comparable to the observations in InAs where the Elliot-Yaffet (EY) [54] mechanism can contribute to the relaxation process. In the EY picture, the strong mixing of the valence band states and conduction bands can result in non-zero transition rates even for spin-conserving scattering process.

In an undoped alloy structure, where equal number of holes and electrons are created after photo-excitation, several scattering mechanisms contribute to the spin relaxation, such as carrier-carrier, carrier-LO phonon and carrier-impurity scattering. The spin-lattice relaxation mechanism due to optical phonons does not work if phonon energy is much higher than the sample's temperature. When hot photo-excited electrons are created initially at low temperatures, there are no equilibrium optical phonons that can contribute to decrease of the relaxation rate. As shown in Fig. 2.6(a) and Fig. 2.6(b), for the SPDT traces at RT and 77 K, we can observe faster spin relaxations at 77 K, in concert with faster carrier relaxation, as shown in Fig. 2.6(c), where the carrier relaxation time scales for RT and 77

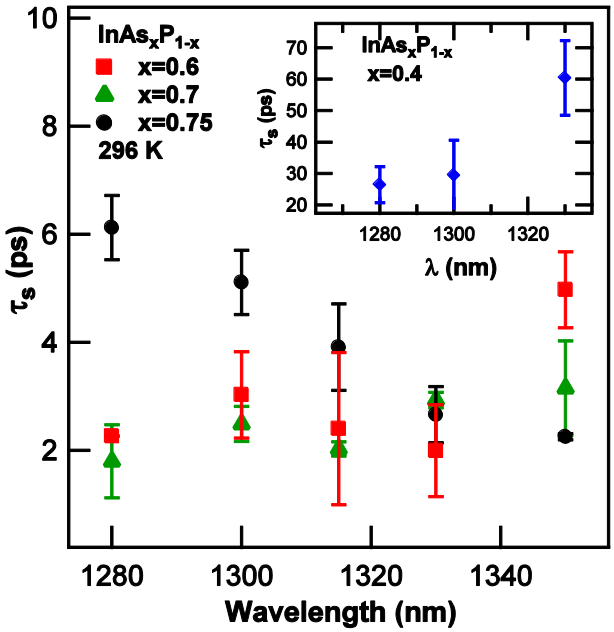

Figure 2.5: Spin relaxation times (τ_s), obtained by the exponential fit of the difference between SCP and OCP curves, versus wavelength for for $x = 0.6$, 0.7, and 0.75. The inset shows the spin relaxation time for $x = 0.4$, ranging from ∼20 to 60 ps.

K are compared.

The inset in Fig. 2.6(c) shows the initial cooling of hot electrons via emission of LO-phonons. In contrast, this component of the relaxation is insignificant at 77 K, and in our samples resulting in a faster spin relaxation time, consistent with the EY mechanism. A similar temperature dependence of spin relaxation for undoped (110) QWs has been reported, suggesting the absence of Dyakonov-Perel (DP) [55] interaction, where the thermal ionization process of excitons with increasing temperature, was considered to be responsible for the increase of τ_s with temperature [56]. The summary of the carrier and spin relaxation times in our samples at 77 K, are presented in Fig. 2.7. Compared to the measurements at RT, the relaxations are faster by a factor of ∼2. For the sample with x=0.4 at 77 K, due to the increase in the band gap, only the pulses tuned at 1270 nm could have been employed and the carrier and spin relaxation times of ∼ 29.0 ps and ∼ 19.0 ps were extracted, respectively.

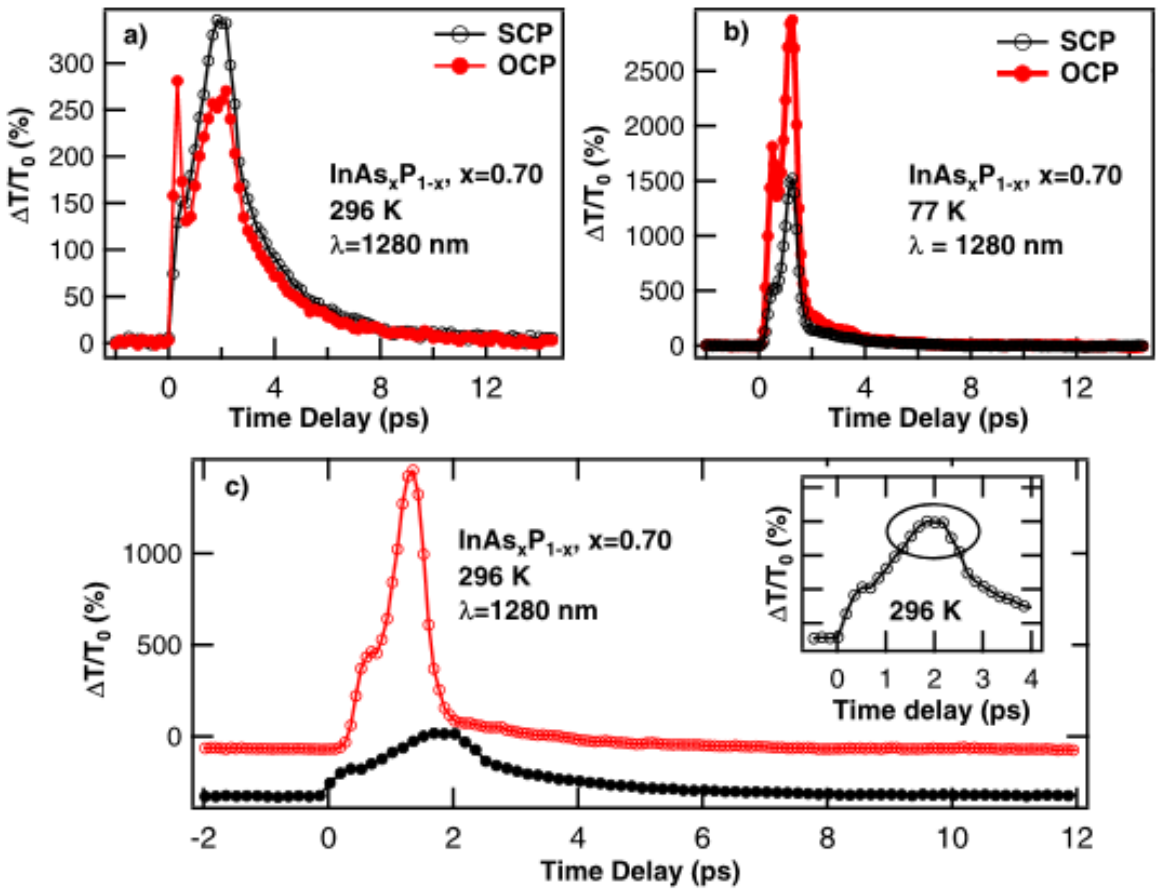

Figure 2.6: Example of spin polarized differential transmission for the sample with $x = 0.7$ at 1280 nm for (a) RT and (b) 77 K. We observe much faster dynamics at 77 K. (c) Carrier relaxation times at RT and 77 K. The faster spin relaxations at 77 K are in concert with a faster relaxation of the photo-excited carriers. As shown in the inset, the initial component of carrier cooling is more important at RT.

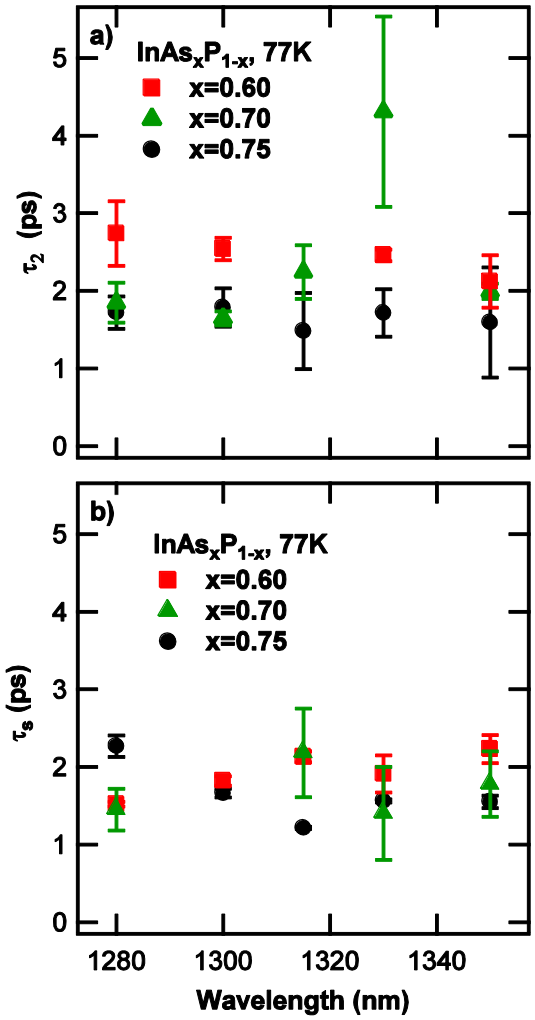

Figure 2.7: (a) Time resolved and (b) spin resolved differential transmission. Both dynamics are faster at 77 K which could be due the absence of LO-phonons. When the hot photo-excited electrons are created initially at low temperatures, there are no equilibrium optical phonons that can contribute to the decrease of the relaxation rate. This fact can result in faster carrier relaxation times it could also have resulted in the observed faster spin relaxations.

2.2 Summary

In summary, we have probed the dynamics of the photo-excited carriers and spins in $InAs_xP_{1-x}$ with different alloy compositions. Our results demonstrate the tunability of the time scales as a function of different external parameters. We observe several carrier relaxation components where the cooling of the photo-excited carriers, via the generation of LO phonons, play an important role and can contribute to the observed time scales of the carrier and spin relaxations in our sample structures.

2.3 Acknowledgments

This work was supported by NSF-Career Award No. DMR-0846834, and by the National High Magnetic Field Laboratory through a UCGP. G. A. Khodaparast thanks the inputs from professor Tigran Shahbazyan and the funding from the Institute of Critical Technology and Applied Sciences (ICTAS) at Virginia Tech. The samples studied in this work were grown and characterized as part of S. G. Choi's Ph.D work at the University of Minnesota.

M. A. Meeker, et al., Phys. Rev. B 92, 125203 (2015).

Chapter 3

High-field magnetic circular dichroism in ferromagnetic InMnSb and InMnAs: Spin-orbit-split hole bands and g factors

M. A. Meeker †, B. A. Magill †, and G. A. Khodaparast [1]

Department of Physics, Virginia Tech, Blacksburg, Virginia, 24061, USA

D. Saha and C. J. Stanton

Department of Physics, University of Florida, Gainesville, Florida 32611, USA

S. McGill

National High Magnetic Field Laboratory,Tallahassee, Florida 32310, USA

B. W. Wessels

Material Research Center, Northwestern University, Evanston, Illinois 60208, USA

[1]Author to whom correspondence should be addressed. Electronic mail: khoda@vt.edu.

Abstract

Carrier-induced ferromagnetism in magnetic III-V semiconductors has opened up several opportunities for spintronic device applications as well as for fundamental studies of a material system in which *itinerant* carriers interact with the localized spins of magnetic impurities. In order to understand the hole mediated ferromagnetism, probing the band structure in these material systems is crucial. Here we present magnetic circular dichroism (MCD) studies on MOVPE grown InMnSb and InMnAs, both with the Curie temperatures above 300 K. The measurements were performed on samples with different Mn contents with the excitation energy tuned from 0.92-1.42 eV and external magnetic fields up to 31 T. The large g-factors in these systems allow us to measure the MCD at relatively high temperatures (190 K). These measurements are compared with MCD calculations based on an eight-band Pidgeon-Brown model, which is generalized to include the coupling between the electron/hole and the Mn spin in a ferromagnetic state. Comparison of the observed MCD with the theoretical calculations provides a direct method to probe the band structure including the temperature dependence of the spin-orbit split-off gap and g-factors, and to estimate the sp-d coupling constants.

3.1 Introduction

Narrow gap ferromagnetic semiconductors (NGFS) such as InMnAs and InMnSb offer promising potential for applications in infrared spin photonics, memory storage, and spin transport devices[57, 58, 59, 60]. Compared to GaMnAs [61], NGFS have smaller band gaps, larger g-factors, and spin-orbit coupling [62, 63], and much higher electron and hole mobilities. The narrow gap materials are also more interesting and difficult to treat theoretically

since there is strong band-mixing between the conduction and valence bands, unlike GaAs where the conduction and valence bands can be treated separately [64, 65].

In the past, low-temperature molecular beam epitaxy(MBE) [57, 58, 66, 67] techniques were nearly exclusively used to prepare NGFS; however, metal-organic vapor phase epitaxy (MOVPE) demonstrated that a single phase NGFS compound could be deposited at 500 °C, much higher than that used in MBE [68, 69, 70]. Furthermore, the MOVPE technique demonstrated that the films are ferromagnetic with a T_c above room temperature (RT) [68, 69, 70]. This is thought to be due to the fact that in MOVPE grown samples, there are local formations of Mn dimers, trimers and tetramers [71, 72] which lowers the hole density and the Fermi Energy. As a result of a lower hole density in the MOVPE grown NGFS, an earlier study estimated that a larger average hole spin polarization, compared to the MBE grown structure, can be achieved [73]. This fact could be responsible for the higher T_c in the MOVPE grown structures. The record T_c of MBE grown GaMnAs is ∼178 K [74] and for MBE grown InMnSb and InMnAs the reported T_c measurements are <10 K and <100 K, respectively [75, 76, 77, 78].

The ferromagnetic films studied in this work, were grown on GaAs (100) substrates using atmospheric pressure MOVPE. These alloys were grown at a substrate temperature of 400 °C to 520 °C at a typical growth rate of 330 nm/hr [68, 70, 79]. The Mn concentration was determined by electron microprobe analysis. All four samples exhibit ferromagnetism with T_C between 330-400 K, as obtained from superconducting quantum interference device measurements.

In our InMnAs films, for Mn concentration equal to or larger than 8%, the ferromagnetism is mainly due to hexagonal MnAs clusters [80]. In case of InMnSb for Mn contents larger than 15%, the temperature-dependent magnetization indicates at least two magnetic phases are present, one with a nominal T_C of 300 K that is attributed to $MnAs_{1-x}Sb_x$ nano-

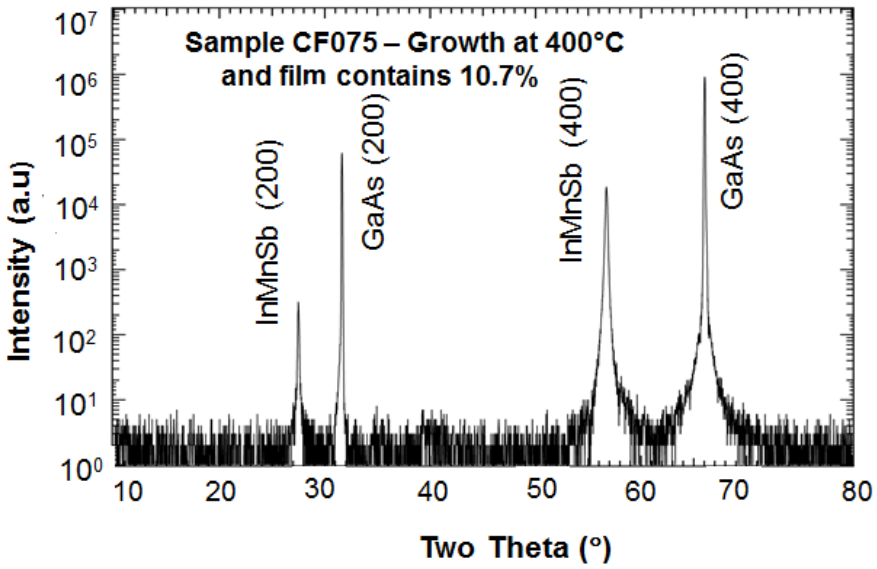

Figure 3.1: The x-ray diffraction of InMnSb with 10.7% Mn demonstrating a single-phase structure. The sample is 500-nm thick, was grown on GaAs, and has a hole density of $1.3 \times 10^{18}\ cm^{-3}$.

precipitates which form at the GaAs substrate interface, and a second with a $T_C > 400$ K that is attributed to hex-MnSb nano-precipitates and to the InMnSb matrix [81, 82]. On the other hand, in the samples studied here, the volume fraction of MnAs or MnSb precipitates, if present, is estimated to be below a volume fraction of 0.1%. As shown in Fig. 3.1, for our InMnSb with Mn=10.7% the structure is a single phase InMnSb.

In this work we report on magnetic circular dichroism (MCD) studies. MCD is a powerful tool for studying ferromagnetic semiconductors where the sp-d coupling between the Mn ions and conduction and valence bands, as well as the band structure can be studied. Our MCD measurements at high magnetic fields were performed at various temperatures (15-190 K), external fields up to 31.25 T, and the excitation energies ranging from 0.92-1.42 eV. Although our measurements were performed relatively far from the Γ point of InMnSb and InMnAs, the large external magnetic fields enhanced our resolution where several transitions

including, the spin-orbit split-off (SO) to conduction band (CB) transitions, were resolved [83]. Recent MCD studies on GaMnAs, in addition to several transport and magnetization measurements, have shown that the location of the Fermi level within the impurity band can play an important role in obtaining T_c [84]. Previous MCD studies on InMnAs and InMnSb aimed to probe the impurity band and the nature of the Mn sp-d interactions [71, 72, 75, 76, 77]. These measurements were performed at low magnetic fields [75, 76, 77, 85], on MBE grown InMnSb structures with the $T_c \approx 10$ K [75, 76, 77, 78, 85] close to the band gap, or on MOVPE grown InMnAs with the T_c of ≈ 330 K, at energies ranging from 1.6 to 3.0 eV [71, 72], .

3.2 Samples:

The samples studied here were MOVPE grown InMnSb and InMnAs structures on GaAs substrates grown at Northwestern University, the details of the growth conditions were described in Refs. [70, 79, 68] and the characteristics of the samples are summarized in Table I.

Table 3.1: Characteristics of the samples studied in this work. The samples are grown on GaAs substrates and in order to avoid damage to the samples, the T_c was not measured above 400 K.

Sample	Density cm^{-3}	Film Thickness nm	x %	Tc K
InMnAs (PTC017)	1.35×10^{18}	600	4	330
InMnAs(PTC015)	1.6×10^{18}	235	2	330
InMnSb(CF009)	2.2×10^{18}	200	4.7	400
InMnSb(CF075)	1.3×10^{18}	500	10.7	400

3.3 MCD Measurements

Our MCD measurements were performed at the National High Magnetic Field Laboratory in Tallahassee, Florida, using the Split Florida-Helix magnet, allowing the temperature to vary between 15-190 K and fields up to 31.25 T. The excitation source was a Quartz Tungsten Halogen lamp with the emitted light being passed through a monochromator set to have a bandwidth of 5 nm. The light was polarized to 45° using a Glan-cube, and the polarization was altered between left and right handed circular polarization by a photo-elastic modulator at 50 KHz. The signal was transmitted through a fiber and detected by a Thorlabs InGaAs detector [PDA20CS]. In order to remove background signals, the MCD presented here is the difference in transmission between right and left handed circular polarizations, averaged over positive and negative fields, and normalized to the intensity of the lamp and the sample thickness: $MCD = \frac{\Delta T(B) - \Delta T(-B)}{2dI_0}$, where T(B) is the magnetic field dependent transmission, B is the external magnetic field, d is the sample thickness, and I_0 is the incident intensity of the lamp. Here, the MCD measurements were presented only on the Mn-doped samples, where the films with no Mn demonstrated a reasonable signal to noise ratio of MCD, at the temperatures below 20 K, which could be related to more randomly distributed impurities in the p-doped n-doped films. An earlier MCD studies on MBE grown InMnSb was compared with a 1.52-mm-thick InSb wafer, available commercially, at 1.8 K [77]. In addition, in case of the MCD study on the MBE grown InMnSb [77] (ranging from 1-5 μm), the dominating transitions were the intra-valence-band transitions from light to heavy holes. The MCD responses were insensitive to external magnetic fields, where both heavy- and light-hole bands shifted in the same direction with changing external magnetic field. In this case [77] only the value of the valence-band exchange constant entered in the modeling of the MCD, while the influence of the conduction-band exchange parameter was not significant. Our MCD study, at high magnetic fields with the probe energy ranging from

0.92-1.42 eV, allowed us to examine the exchange coupling parameters both in the valence and conduction band using the model described later in this paper.

3.3.1 InMnSb

Figure 3.2 shows a typical MCD trace for the two different InMnSb films. The MCD spectra display a broad positive background signal throughout the range as well as an oscillatory like behavior. The oscillations are not due to Fabry-Perot interference, as shown in the inset of Fig. 3.2, no oscillatory pattern was observed for the transmission through the samples, at the same magnetic field. Previous MCD measurements on MBE grown InMnSb showed small peaks around 1000 nm (1.24 eV) [76, 85] at low magnetic fields while a different MCD study, has shown a relatively broad peak centered at $\sim$ 1250 nm (0.992 eV) [75].

In this study, the magnetic field dependence of the MCD response was measured and an example of the field dependence for CF009 (InMnSb with 4.7% Mn) is shown in Fig. 3.3. As the magnetic field increases, the amplitude of MCD increases and blue shifts in energy, while the overall shape remains the same. This fact can be described in a simple picture sketched in Fig. 3.4. As shown in panel (a), due to the Zeeman splitting, the spin degeneracy is lifted, and in this case shifting the $|HH\downarrow>$ and $|LH\downarrow>$ bands to a higher energy, as a result, the two spin states will be above the Fermi energy and can only have contributions to MCD transitions at higher energies. In Fig. 3.4(b), the density of states, for a quasi-one-dimensional system, is presented. As shown in by red dashed line, the net MCD can be extracted by taking the sum of the contributions from the HH and LH bands with different spins. When the magnetic field increases, the splitting of the bands become larger, and therefore the lowest energy transition becomes higher in energy, possibly leaving those bands completely above the Fermi energy. This will result in reduced contributions from

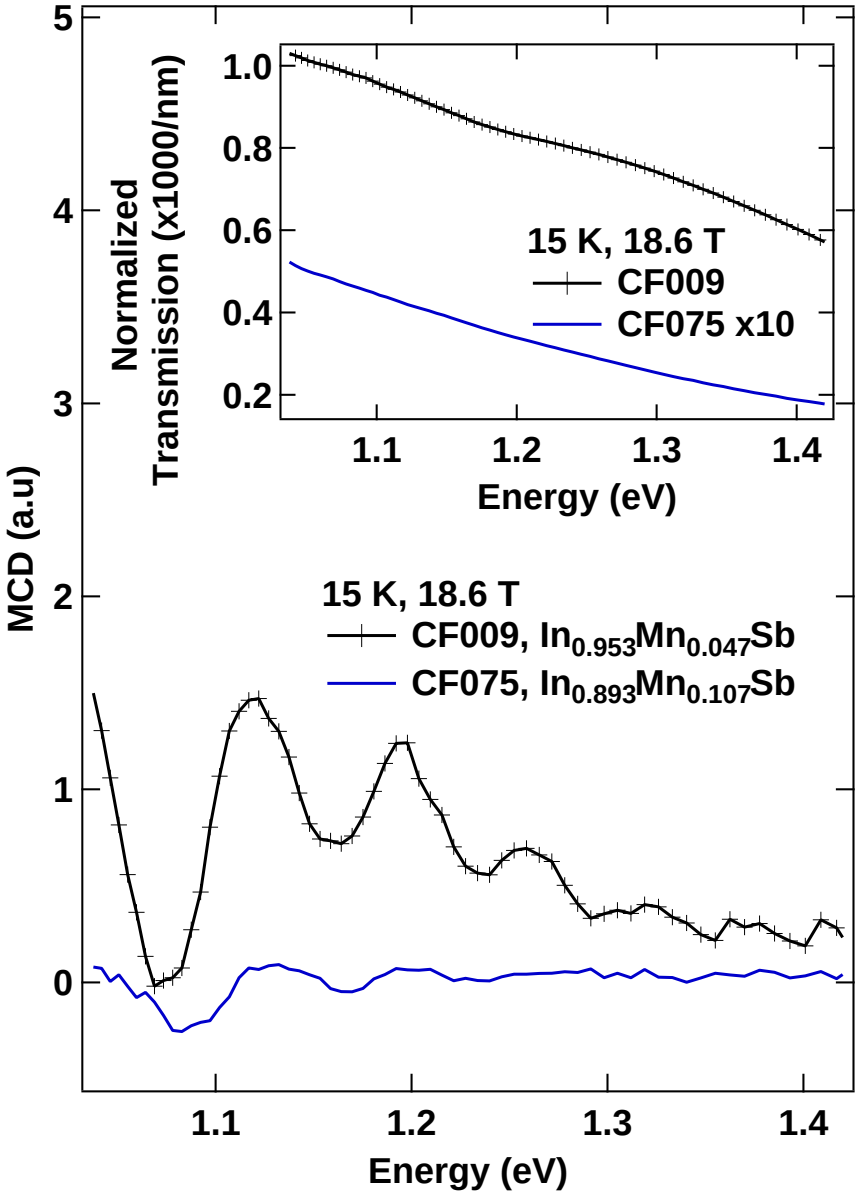

Figure 3.2: (Color online) The MCD spectra of the two InMnSb structures with different Mn content. The oscillations in the MCD spectra are related to several interband transitions. As shown in the inset, the oscillations are not due to interference as they are absent in the transmission through the samples when the detected signal was not polarized.

these states and increases the MCD signal until higher energy effects not shown here, such as Landau levels, start to contribute. Our magnetic field dependence MCD measurements show the strong increase in the magnitudes and the expected blue shifts.

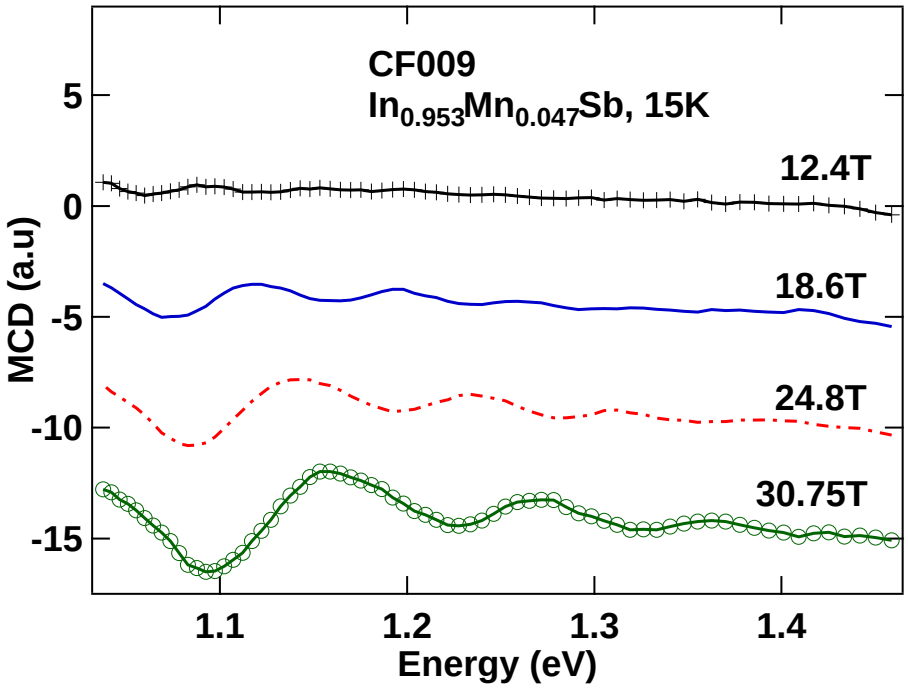

Figure 3.3: (Color online) The Magnetic field dependence of the MCD spectra for the InMnSb (CF009, with Mn = 4.7%) at 15 K as a function of the excitation energies is presented here. The MCD is resolved more significantly at high fields where the blue shift is expected as a result of larger band splitting at higher fields. The peaks are shifted for clarity.

3.3.2 InMnAs

Figure 3.5 shows examples of MCD transitions for $In_{0.96}Mn_{0.04}As$ (blue) and $In_{0.98}Mn_{0.02}As$ (black) at ∼60 K and ∼ 31 T. The MCD response from both structures displays a similar pattern, with a small blue shift for the higher Mn contents. While the various maxima and minima are distinct at lower energies (0.92-1.1 eV), when examining the field dependance of

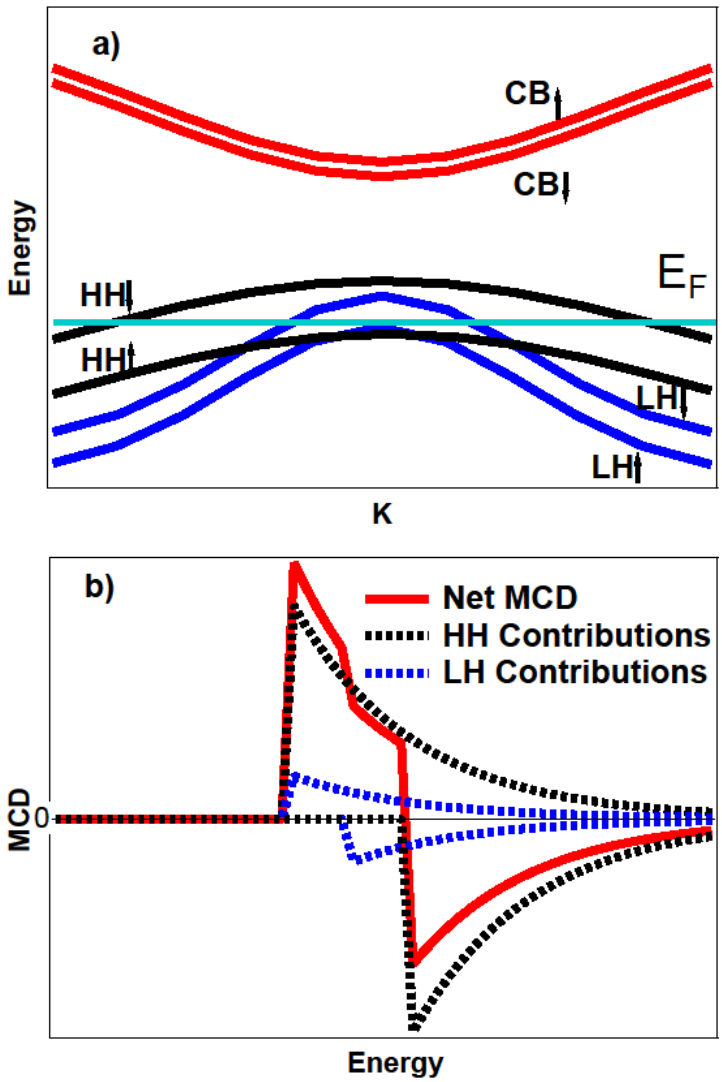

Figure 3.4: (Color online) (a): A simplified picture of the band structure for a semiconductor in a magnetic field. The $|\downarrow\rangle$ spin states are partially above the Fermi energy, represented by the light blue line. (b) The density of states for a quasi one dimensional system where a bulk structure is placed in an external magnetic field. The contributions to the MCD can be seen in (b), with the partial contributions arising from regions identified by the dashed lines, and the full contribution from regions identified by the solid line.

the MCD response in Fig. 3.6, the peaks start to become more asymmetric and finally, as the field increases to 31 T, the splitting of the peaks are more distinct.

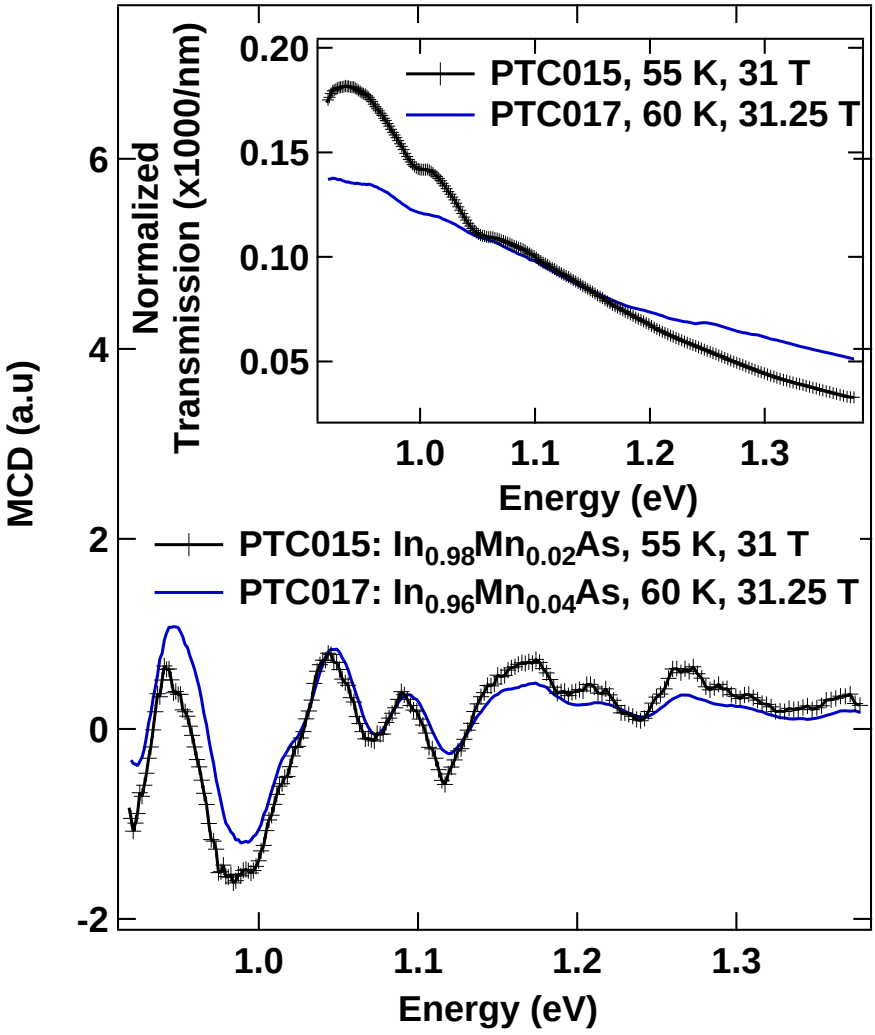

Figure 3.5: (Color online) The MCD spectra of InMnAs with 2% and 4% Mn contents at 55 K, 31 T and 60 K, 31.25 T, respectively. At lower energies, the peaks are more distinct, however as the excitation energy increases, the peaks start to convolute. The inset shows the transmissions through the samples at fixed magnetic fields.

3.4 Theoretical Calculations and Modeling

Our theoretical model is based on an 8-band $\mathbf{k}\cdot\mathbf{p}$ Pidgeon-Brown model [86] for a narrow gap semiconductor in a static magnetic field parallel to the z-direction B_z. Elements of the

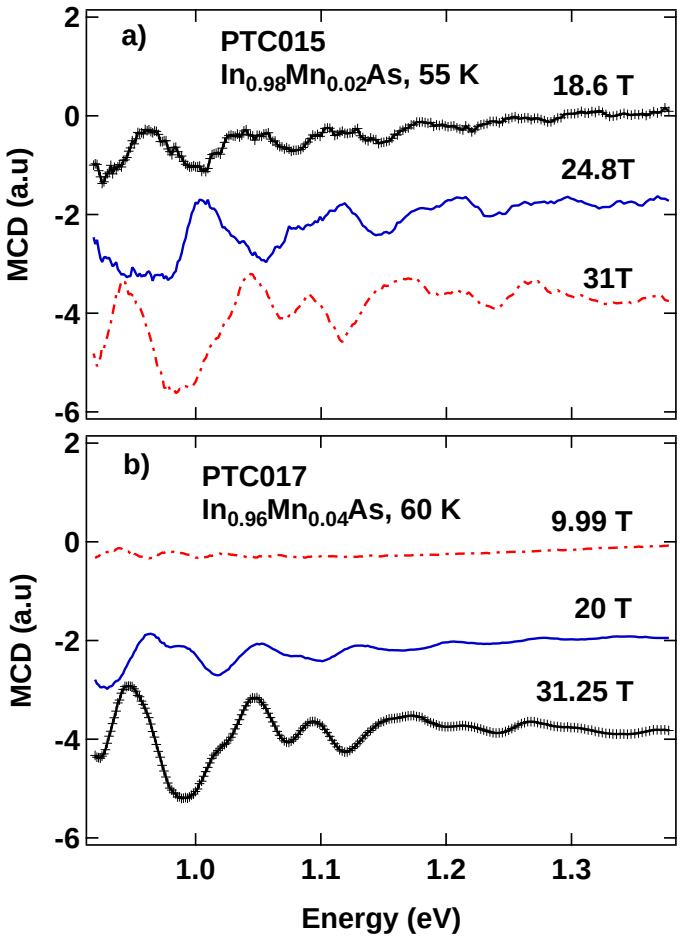

Figure 3.6: (Color online) (a) The field dependance of MCD for $In_{0.98}Mn_{0.02}As$. As the field increases, the lowest energy peak at 18.6 T starts to blue shift and becomes more asymmetric. As the field is increased further, the peak blue shifts and starts to form a double structure. (b) The field dependance of $In_{0.96}Mn_{0.04}As$. Similar to the $In_{0.98}Mn_{0.02}As$, the evolution of MCD response, with increasing the field, shows blue shifts and the formation of double peaks.

model have been described in great detail elsewhere [87, 88, 89, 90]. Here we summarize the salient features of the model. In our model, since these are three dimensional, bulk systems, the wavevector k_z in the direction of the magnetic field is still a good quantum number and we include the full (k_z) wave vector dependence of the itinerant electronic states. We also allow for the *sp-d* coupling of the itinerant conduction band electrons and valence band holes to the localized d electrons in the Mn ion cores. We separate the eight Bloch basis states

into an upper and lower set of four Bloch basis states which decouple at the zone center, i.e. $k_z = 0$. The Bloch basis states for the upper set are $|S\uparrow\rangle$, $|HH\uparrow\rangle$, $|LH\downarrow\rangle$ and $|SO\downarrow\rangle$, which correspond to electron spin up, heavy-hole spin up, light-hole spin down, and split-off hole spin down, respectively. Similarly, the Bloch basis states for the lower set are $|S\downarrow\rangle$, $|HH\downarrow\rangle$, $|LH\uparrow\rangle$, and $|SO\uparrow\rangle$ corresponding to electron spin down, heavy-hole spin down, light-hole spin up, and split-off hole spin up. The explicit expressions for these 8 Bloch basis states are given in [87, 88, 89]. The total effective mass Hamiltonian is the sum of the Landau (H_L), Zeeman (H_Z), and *sp-d* exchange (H_{ex}) contributions, *i.e.*

$$H = H_L + H_Z + H_{ex} \tag{3.1}$$

Explicit expressions for these Hamiltonians are given in Ref. [87, 88, 89]. The parameters that we use for the model are given in Table 3.2.

We used the standard Luttinger parameters [83] and temperature-dependent energy gaps for InSb and InAs as inputs in the Landau and Zeeman Hamiltonians. In the Mn exchange Hamiltonian, H_{ex}, of Eq. (3.1), we follow the method of Kossut [91] and include the effects of the spontaneous magnetization of the Mn ions (magnetic impurities) and the coupling of this magnetization to the conduction band electrons and valence band holes through the s-d and p-d exchange interactions. The values of the exchange constants for the *s-d* interaction, $N_0\alpha$, and *p-d* interaction, $N_0\beta$, are taken to be -0.5 eV and 1.0 eV, respectively [92]. The spontaneous magnetization depends on the Mn concentration x, and the z component of the average Mn spin $\langle S_z\rangle$. In determining the z component of Mn spin, we can allow for the system to be either paramagnetic or ferromagnetic, this is described in Refs. [65, 93]. The spin of the Mn ions is calculated using mean-field theory, with $\langle S_z\rangle$ determined from

Table 3.2: Material parameters for InMnAs and InMnSb Ref. [83].

Parameter	InMnAs	InMnSb
Energy gap		
E_g^{Γ}(eV, $T = 0$)	0.417	0.235
Electron effective mass		
m_e^*/m_0 ($T = 0$)	0.026	0.0135
Luttinger parameters		
γ_1^L	20.0	34.8
γ_2^L	8.5	15.5
γ_3^L	9.2	16.5
Spin-orbit splitting		
Δ (eV)	0.39	0.81
Optical matrix parameters		
E_p (eV)	21.5	23.3
s-d and p-d exchange energies (eV)		
$N_0\alpha$	-0.5	-0.5
$N_0\beta$	1.0	1.0

$$\langle S_z \rangle = SB_s\Big\{\frac{gS}{kT}\Big[\mu_B B - \frac{3kT_c\,\langle S_z\rangle}{gS(S+1)}\Big]\Big\}, \tag{3.2}$$

where g is the free electron g factor, B_s is the Brillouin function, and S = 5/2 is the spin of the magnetic Mn ion. The temperature T and the T_c depend on the measurements and the samples.

The values of x in our calculations are taken to be the Mn fraction in the actual samples as experimentally reported. The value of $\langle S_z \rangle$ is determined in the mean-field approximation using the lattice temperature T and the Curie temperature, T_c, of the samples from Table I as inputs. With the inclusion of ferromagnetic ordering of the Mn ions, the spontaneous magnetization and its *sp-d* coupling to the itinerant carriers will spin-split the bands even in the absence of an external magnetic field.

In calculating the electronic structure with B$\neq$ 0, to simplify the results, we make the *axial approximation* where we replace γ_2 and γ_3 by their average $(\gamma_2 + \gamma_3)/2$. This decouples the Pidgeon-Brown manifolds meaning that the Landau levels can be obtained by diagonalizing an 8×8 Hamiltonian (or smaller) for each Pidgeon-Brown manifold. For B = 0, we do not need to make this approximation and we can view the full anisotropic bands. This is shown in Fig. 3.7(a) for InMnSb and Fig. 3.8(a) for InMnAs, where we plot the bands for B = 0, T = 15 K in both the [001] and [111] directions. We see that the bands are already spin-split even without the application of an external magnetic field since the two samples are ferromagnetic. In Fig. 3.7(b) and Fig. 3.8(b), we plot the Landau levels as a function of k_z for the InMnSb and InMnAs samples, respectively. In each figure, the red lines represent the transitions that are possible for 1.0-eV excitation and the blue lines represent the transitions possible for 1.5-eV excitation. We see that for 1.0 eV excitation, the SO to CB transition is not energetically possible, but it is possible once the excitation energy reaches the band gap between the SO and CB gap, which occurs below 1.1 eV (green line).

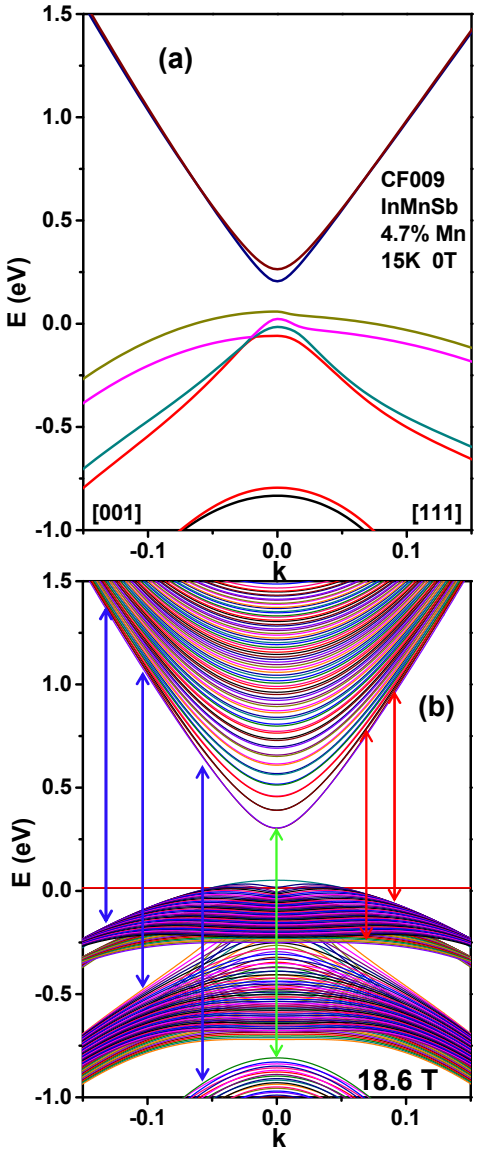

Figure 3.7: (Color online) The electronic structure for InMnSb (with Mn = 4.7%) at 15 K (sample CF009). (a) Electronic structure with B = 0 in the [001] and [111] direction. The bands are spin split owing to the ferromagnetism of the sample. (b) The electronic structure for B = 18.6 T as a function of k_z showing the Landau levels structure. Red arrows show the approximate allowed transitions for excitation with a 1.0 eV and the blue arrows show the allowed transitions for a 1.5-eV excitation. We see that the SO to CB is not possible for 1.0-eV excitation. This transition first becomes allowed below 1.1 eV (green arrow).

This is in contrast to InMnAs where the SO split transition is possible for 1.0-eV excitation (even though the band gap is larger for InMnAs than for InMnSb, the SO splitting is smaller, and hence the SO to CB transition occurs at a smaller energy).

We note that at $k_z = 0$, we can calculate the *relative strengths* of the valence band to conduction band transitions for circularly polarized light. This is shown in Table 3.3. From the wave functions given in the table, we see that the ratio of the squares of the matrix elements (which gives the relative strengths of the transitions) for the HH, SO, and LH to CB transitions, for circularly polarized lights are $3 : 2 : 1$, with the SO and LH transitions producing the opposite CB spin polarization than the HH transition. In the table, P is the momentum matrix element $P \equiv \langle S| P_x |X\rangle = \langle S| P_y |Y\rangle = \langle S| P_z |Z\rangle$.

To determine the optical properties, we use Fermi's golden rule to calculate the magneto-absorption. The absorption can be calculated for both σ^+ and σ^- circularly polarized light and if we subtract the two contributions, $\alpha_{\sigma^+} - \alpha_{\sigma^-}$, we can generate the MCD response. Figure 3.9 shows the comparison of the experimental MCD and the model for the two InMnSb films. We assigned the first transitions, below 1.1 eV to the SO-CB, and the higher energy MCD responses, to several possible valence band transitions. The model described here provides a better fit the film with 4.7% compared to the film with 10% Mn content.

Figure 3.10 shows the magnetic field evolution of the MCD for the InMnAs film with 2% Mn content from 12.4 T to 31 T. The small features grow as the magnetic field increases and our model maps even these observed small features. As summarized in Table 3.2, the s-d and p-d coupling parameters are kept the same for both InMnAs and InMnSb and the other parameters were selected from the accepted parameters for bulk InSb and InAs. The broadenings in the transitions were used as an input parameter.

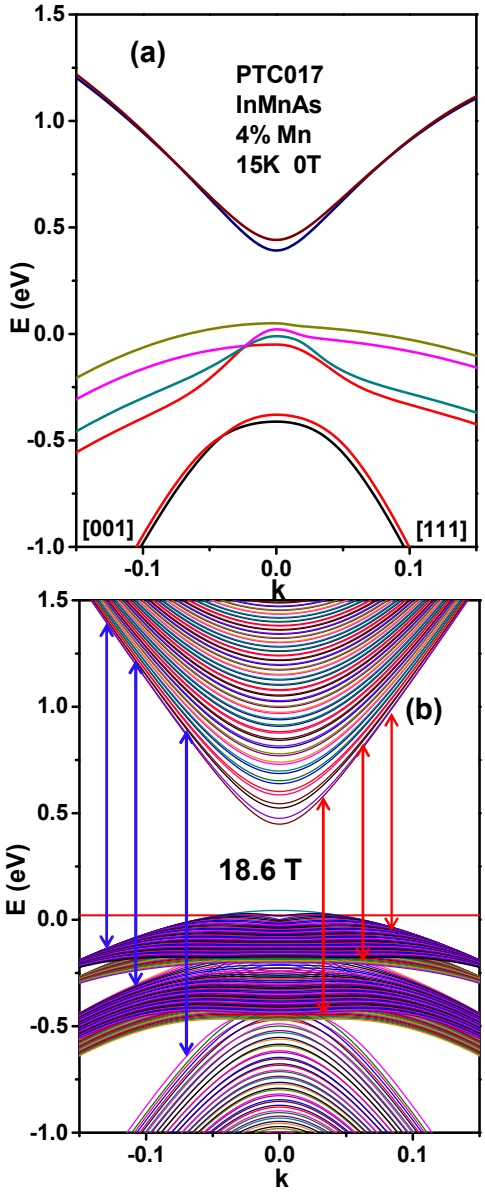

Figure 3.8: (Color online) The electronic structure for InMnAs (with 4.0% Mn) at 15 K (sample PTC017). (a) Electronic structure with B = 0 in the [001] and [111] direction. The bands are spin-split owing to the ferromagnetism of the sample. (b) The electronic structure for B = 18.6 T as a function of k_z showing the Landau levels structure. Red arrows show the approximate allowed transitions for excitation with a 1.0-eV excitation and the blue arrows show the allowed transitions for a 1.5-eV excitation. Unlike InMnSb, we see that the SO to CB transition *is allowed* for 1.0-eV excitation. While the band gap for InMnAs is larger than for InMnSb, the SO splitting Δ is smaller and thus the SO to CB transition is allowed at 1.0 eV.

Table 3.3: Relative strength of valence band to conduction band transitions for circularly polarized light.

Circ. Pol.	Hole State	Conduction Band State	Transition Strength
	$\|HH\uparrow\rangle$	$\|C\uparrow\rangle$	P^2
	$\frac{1}{\sqrt{2}}\|(X+iY)\uparrow\rangle$	$\|S\uparrow\rangle$	
	$\|LH\uparrow\rangle$	$\|C\downarrow\rangle$	$\frac{1}{3}P^2$
σ^-	$\frac{i}{\sqrt{6}}\|(X+iY)\downarrow -2Z\uparrow\rangle$	$\|S\downarrow\rangle$	
	$\|SO\uparrow\rangle$	$\|C\downarrow\rangle$	$\frac{2}{3}P^2$
	$\frac{1}{\sqrt{3}}\|(X+iY)\downarrow +Z\uparrow\rangle$	$\|S\downarrow\rangle$	
	$\|HH\downarrow\rangle$	$\|C\downarrow\rangle$	P^2
	$\frac{i}{\sqrt{2}}\|(X-iY)\downarrow\rangle$	$\|S\downarrow\rangle$	
	$\|LH\downarrow\rangle$	$\|C\uparrow\rangle$	$\frac{1}{3}P^2$
σ^+	$\frac{1}{\sqrt{6}}\|(X-iY)\uparrow +2Z\downarrow\rangle$	$\|S\uparrow\rangle$	
	$\|SO\downarrow\rangle$	$\|C\uparrow\rangle$	$\frac{2}{3}P^2$
	$\frac{-i}{\sqrt{3}}\|(X-iY)\uparrow +Z\downarrow\rangle$	$\|S\uparrow\rangle$	

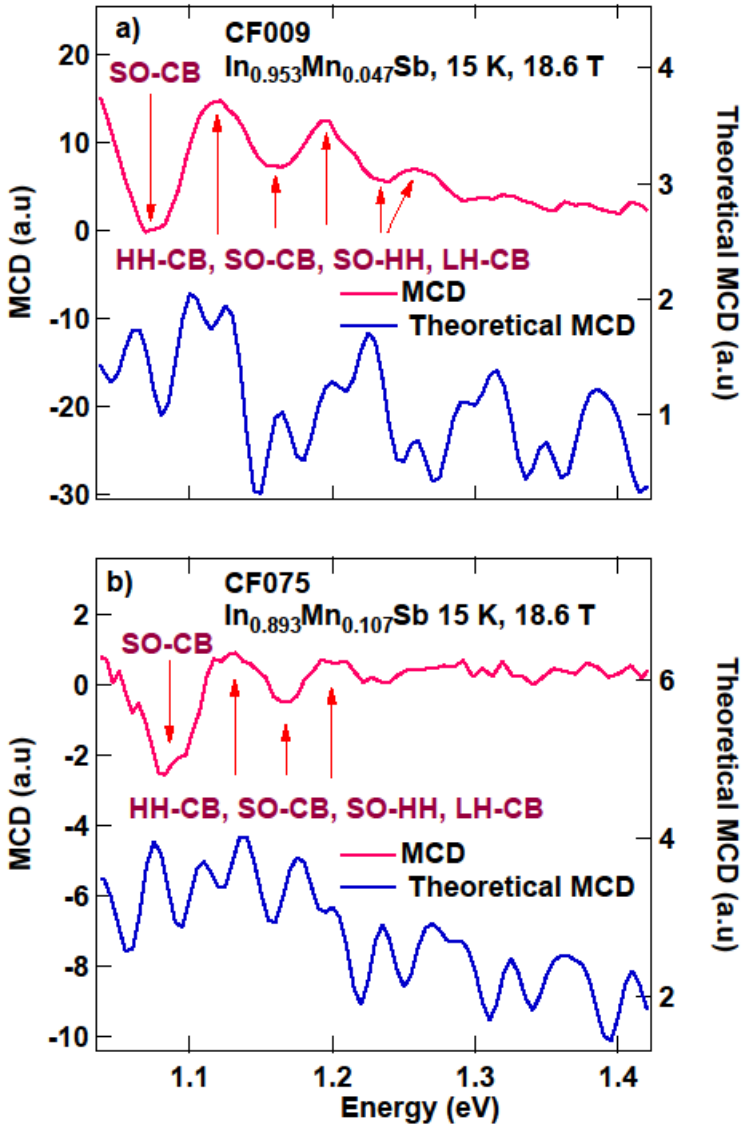

Figure 3.9: (Color online) The theoretical model and the experimental MCD responses of the two InMnSb films, CF009 and CF075 at 15K and 18.6 T. The model can describe the features in the (a) for 4.7% Mn content better than the sample with 10% Mn in (b).

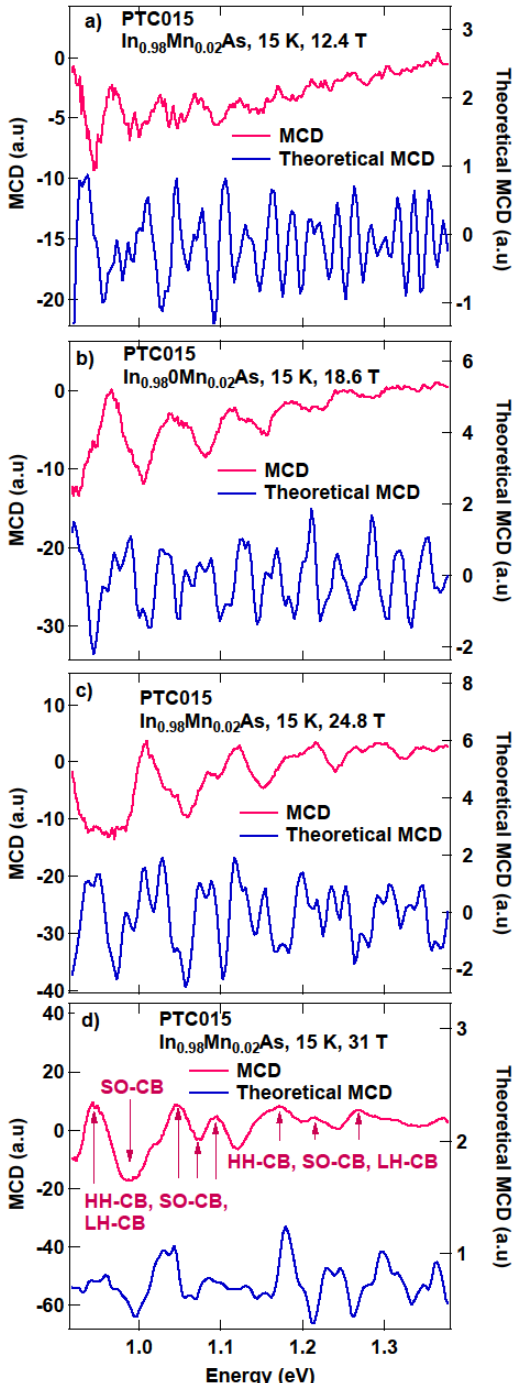

Figure 3.10: (Color online) A comparison between the theoretical MCD (blue) and experimental MCD (red) at 15 K and (a) 12.4 T (b) 18.6 T (c) 24.8 T, (d) 31 T. The theoretical MCD matches the observed MCD features, the broadening of the transitions was adjusted to provide the best fit. The small features grow as the magnetic field increases and our model maps this evolution accurately.

3.5 Temperature Dependence

3.5.1 InMnAs

Aside from the magnetic field-dependance measurements, the temperature dependance was also taken as shown in Fig. 3.11. In Fig. 3.11, the MCD was normalized by the value of the MCD at 0.992 eV for both samples (the traces are shifted for clarity after the normalization). Since the transition probability is independent of temperature, the MCD should scale with temperature if it originates only from one transition. Therefore if the MCD is normalized by the MCD at a certain point, we should be able to determine if each peak is the result of a single or multiple transitions [72, 94]. The normalized MCD shown in Fig. 3.11 (a) and (b), clearly demonstrate the shifts in the individual peak position, thus the peaks are due to a composition of a response from multiple transitions. This temperature dependance has been reflected both in the experimental observation and the presented model in Fig. 3.10. Earlier studies reported in Ref. [72] observed a similar temperature dependence of their main observed MCD transitions in an MOVPE grown InMnAs.

3.5.2 InMnSb

As stated earlier, if the MCD is caused by a single transition, then the temperature dependence would only scale the spectra, whereas a shift in the peak position could be the consequence of multiple transitions [71, 94]. This process can be seen in the transition from Fig.3.12(a) to Fig. 3.12(b); the latter presents the MCD of the InMnSb with 4.7% Mn (CF009) normalized to its value at 1.117 eV (the traces are shifted for clarity after the normalization). As the MCD spectra clearly shows more complex behavior than scaling, the resulting MCD is due to multiple transitions where our excitation energy range

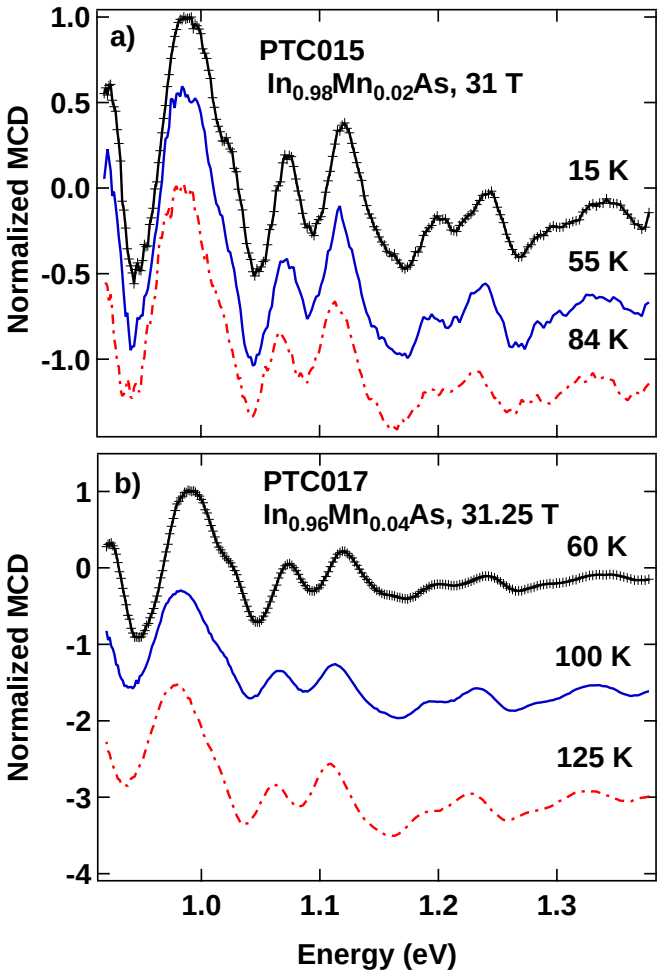

Figure 3.11: (Color online) Temperature dependence of (a) $In_{0.98}Mn_{0.02}As$ at 31 T and (b) $In_{0.94}Mn_{0.04}As$ at 31.25 T. In order to determine whether each peak is due to a single or multiple transitions, we normalized the MCD to the value of the MCD at 0.992 eV. For both samples the peaks shift with temperature implying that the individual peaks are due to multiple transitions, as the temperature dependence of the band gaps cannot be entirely explained by the shifts.

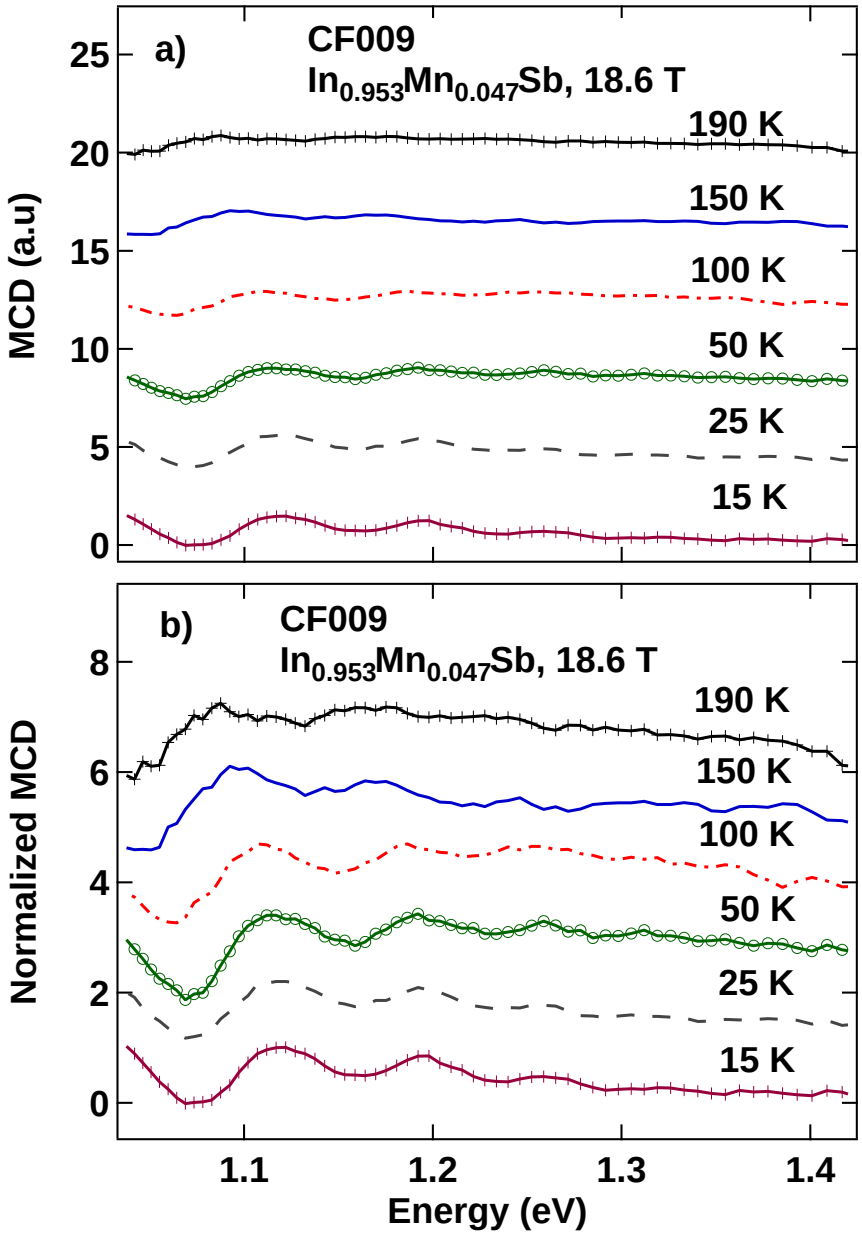

Figure 3.12: (Color online) (a) The temperature dependence of the InMnSb sample (CF009) with 4.7% Mn at 18.6 T. (b) In order to determine if the MCD is comprised of a single or multiple transitions, the MCD at each temperature was normalized to the MCD at 1.117 eV. The temperature dependence of the band gaps cannot entirely explain the shifts in the individual peaks.

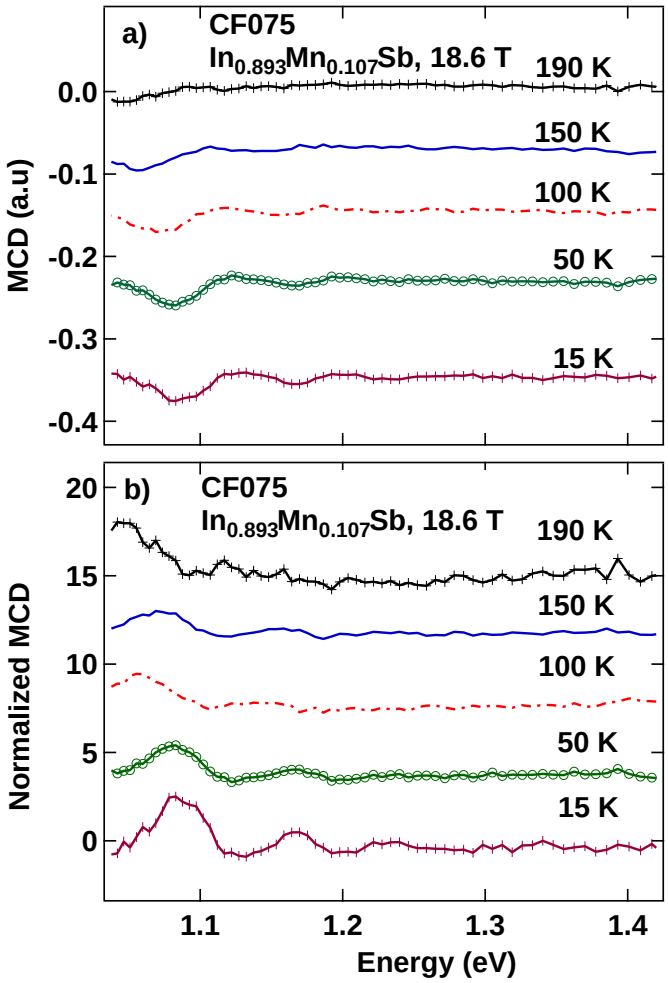

Figure 3.13: (Color online) (a) The temperature dependence of the InMnSb sample (CF075) with 10.7% Mn at 18.6 T. (b) In order to determine if the MCD is comprised of a single or multiple transitions, the MCD at each temperature was normalized to the MCD at 1.069 eV .

allowed multiple transitions from the valence bands to the CB. This is supported by the theoretical model in which multiple transitions can be seen near each of the observed peaks. Furthermore, the peak at $\sim$ 1.08 eV at 15 K and 18.6 T for the CF009 sample originate from SO-CB transition. A similar normalization was done for the MCD response of the sample with 10.7% Mn, as shown in Fig. 3.13(b), where in order to determine if the MCD is comprised of a single or multiple transitions, the MCD responses in Fig. 3.13(a), at each temperature, were normalized to the MCD at 1.069 eV (the traces are shifted for clarity after the normalization).

3.6 SO-CB gap and Varshni Coefficients

The MOVPE grown InMnSb samples have a large peak below 1.1 eV and the InMnAs samples have a large peak below 1 eV at $\sim$15 K and 18.6 T. We assign these peaks to the SO to CB transitions, which is at 1.045 eV at 0 K for InSb and 0.807 eV for InAs [83]. One might question why we assign this to the SO-split rather than the HH-band transition, since the HH transition is stronger, according to Table 3.2. It is important to note though, that the results in Table 3.2 hold only for the $k = 0$ basis functions of the state. Away from $k = 0$, band-mixing effects can decrease the strength of the transitions. Our band structure calculations suggest that only one valence band (corresponding to the p = -1 Pidgeon-Brown manifold) is a pure HH state, corresponding to the $n = 0$ Landau level, for the HH spin-down state. When one goes to higher Landau levels (even at $k = 0$) there is strong mixing between the HH and LH, which reduces the strength of the transitions. In addition, as one goes to higher excitation energy, the transitions occur for larger and larger values of k_z which also increases the mixing. Also, there is a *density of states* effect (for the one-dimensional density of states associated with the k_z quantum number in the direction of the magnetic

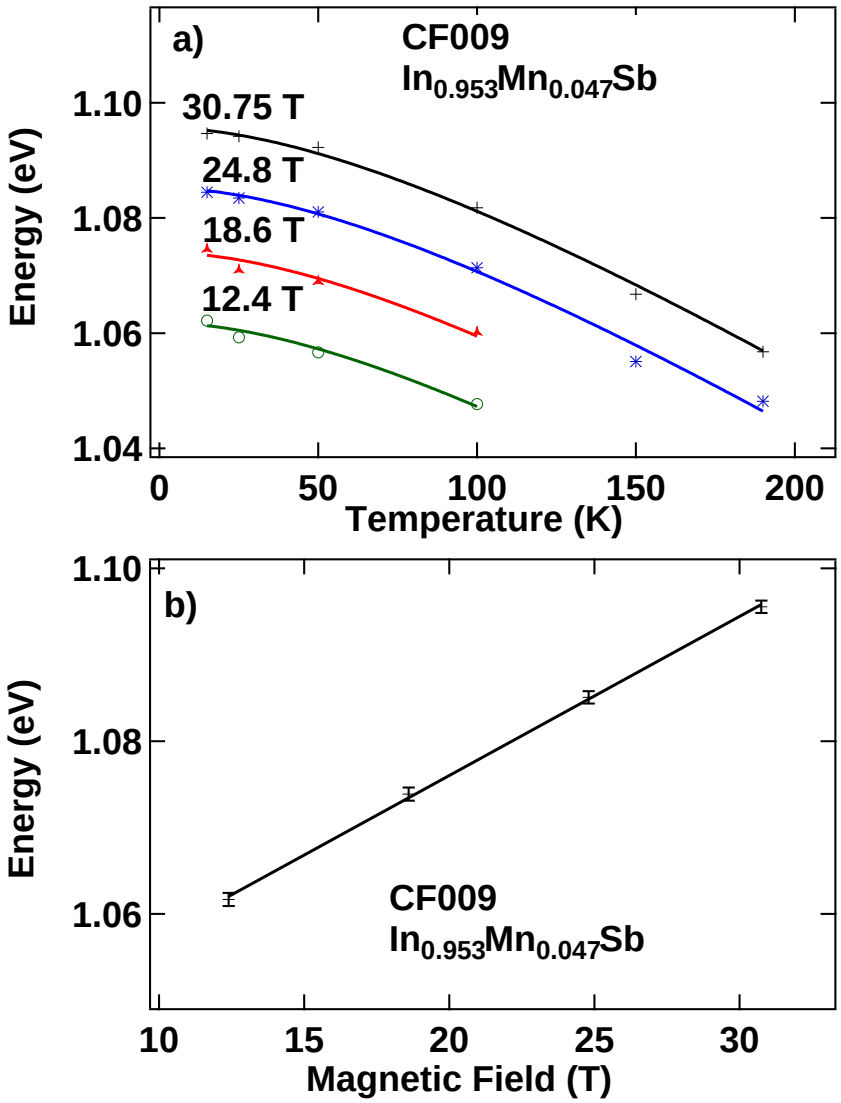

Figure 3.14: (Color online) In order to find the SO to CB gap, we fit the evolution of the peak at $\sim$ 1.07 eV at 15 K at 18.6 T, for InMnSb (CF009, 4.7% Mn), at various temperatures and magnetic fields. As shown in (a) the temperature dependence of the transition was fit to the Varshni equation, with the constraints that A and B were the same for all of the fields. (b) These gaps were plotted vs the magnetic fields and from a linear fit the gap of 1.0392$\pm$0.00075 eV at zero field can be estimated.

Table 3.4: The spin-orbit (SO) to conduction-band (CB) gap and the Varshni coefficients (A and B) in InMnSb and InMnAs compared to InSb and InAs.

Sample	$E_{SO->CB}(0)$ (eV)	A (meV/K)	B (K)
$In_{0.953}Mn_{0.047}Sb$	1.0392 ± 0.0012	0.37± 0.06	155±56
InSb Ref.[83]	1.045	0.32	170
$In_{0.98}Mn_{0.02}As$	0.85635	0.18	137
InAs Ref.[83]	0.807	0.276	93

field), which varies as $1/\sqrt{(E)}$ or $1/k$ and makes the $k = 0$ transitions the strongest. We note that in contrast to the HH and LH transitions, the SO transition initially occurs when $k = 0$ and these states are almost pure SO states and have less mixing, *i.e.* they are $\sim 98\%$ SO. Mixing is also less for the SO states since they are not initially degenerate with the LH and HH states. Finally, we also point out that the initial HH and LH Landau levels (near $k = 0$) lie above the Fermi level so these transition are not possible.

By assigning the peak at ∼1.08 eV at 18.6 T, 15 K for InMnSb (CF009) to the SO to CB transition, we can use the magnetic field and temperature dependence to extract the gap between the SO band and the CB. An example of magnetic field dependence at 15 K is shown earlier in Fig. 3.3. As expected, the peak's amplitude increases and the peak blue shifts with increasing field. The peak position was calculated by a Gaussian fit, and the position for each magnetic field was plotted vs temperature in Fig. 3.14(a). Similar to the modeling of the fundamental gap, the points were fit to the Varshni equation $E_g(0) = E_g(T) + \frac{AT^2}{B+T}$, with A and B being 0.37 meV/K and 155 K, respectively. These values are close to the recommended values from Ref. [83] to be 0.32 meV/K and 170 K. As shown in Fig. 3.14(b), the resulting SO gaps were plotted as a function of the magnetic field and fit to a line, giving a y intercept of 1.039±0.00075 eV, which is close to the expected 1.045 eV SO gap in bulk

InSb. We used the same procedure for the InMnAs, and Table 3.4, summarizes the extracted SO-CB gaps as well as Varshni coefficients for InMnSb and InMnAs.

3.7 Conclusions

The large g factors in the narrow gap InMnSb and InMnAs systems allow us to measure the MCD at relatively high temperatures. Our experimental measurements were compared with MCD calculations based on an eight-band Pidgeon-Brown model extended to include the effects of the Mn impurities and the $sp-d$ exchange interaction and allowed for ferromagnetic order of the Mn ions. A comparison of our experimental and theoretical results show that the dominant structure in the MCD spectrum *in this energy range* comes from the *split-off hole to conduction band transitions.* This is somewhat surprising since one usually thinks of the HH to CB band as being a stronger transition. In this case, the SO to CB transition was the strongest for a variety of reasons: (i) as shown in Fig. 3.7 and Fig. 3.8 in this energy range, the HH and LH band transitions occur in the higher Landau levels and also away from $k_z = 0$. As a result, HH and LH transition states are heavily mixed. (ii) For k_z away from 0, there is a density of states effect which decrease the strength of the transition. (iii) The SO transition occurs near $k_z = 0$, where there is little mixing. In addition we don't identify any transitions that could be associated with the impurity bands.

From our band structure calculations, it can be seen that the SO-CB transition occurs at an energy slightly higher (lower) than 1.0 eV for InMnSb (InMnAs). The largest peak for InMnSb (at $\sim$ 1.08 eV at 15 K and 18.6 T) was fit to the Varshni equation, which lead to parameters close to the earlier reported values for InSb [83]. Since for InMnSb the SO-CB transition dominates, we were able to use the field dependence of the largest transition peak (SO$\rightarrow$CB) to extract the difference in the g factor between the SO and CB bands. In order

Table 3.5: The temperature dependent of Δg for InMnSb and InMnAs.

Temperature (K)	InMnSb Mn=4.7% Δg	InMnSb Mn=10% Δg	InMnAs Mn=2% Δg
15	31.9	46.3	86.4
25	31.55		
50	31.7	26.75	
55			78.0
84			81.8
100	30.91		
150	28.27		
190	29.06		

to find the difference in g factor, the peak position of each sample, at a given temperature was plotted as a function of the magnetic field. The peak positions were fit to the equation E=ΔgμB+E_0, where E is the peak position at different fields, Δg is the difference in the CB and SO g factors, μ is the Bohr magneton, and E_0 is the SO-CB gap at zero magnetic field. Due to the limits in our energy range, the Δg for $In_{0.96}Mn_{0.04}As$ could not be determined. The resulting values for the other three samples are summarized in Table 3.5. The Δg-factor is relatively constant throughout the temperature range for $In_{0.953}Mn_{0.047}Sb$.

3.8 Acknowledgments

This work was supported by the AFOSR through Grant FA9550-14-1-0376. In addition, (GK,BM,MM) were supported by NSF-Career Award DMR-0846834 and (BW) was supported by NSF-DMR-60035274 and NSF-DMR-1305666. S.M. acknowledges support from the NSF MRI program (DMR-1229217). A portion of this work was performed at the National High Magnetic Field Laboratory, which is supported by National Science Foundation

Cooperative Agreement No. DMR-1157490 and the State of Florida.

M.A.M and B.A.M have contributed equally to this work.

Chapter 4

Reflectometry measurements of valent doped barium titanate

4.1 Abstract

While ferroelectric materials offer great potentials for nonvolatile random access memory, commonly implemented ferroelectrics contain lead. One promising candidate for lead-free ferroelectric based memory is (1-x)$BaTiO_3$-xBa($Cu_{1/3}Nb_{2/3}$)O_3 (BT-BCN), x=0.025. The samples studied here were grown on a Si substrate with a HfO_2 buffer layer, preventing the interdiffusion of Si into the sample layer. The sample thicknesses ranged from 1.5-600 nm, and piezoelectric force microscopy was employed in order to demonstrate ferroelectric behaviors. Reflectometry was performed in order to determine the refractive index for three samples with differing thicknesses, and we report refractive indices similar to that of barium titanate.

4.2 Introduction

Ferroelectric (FE) materials are promising candidates for random access memory devices due to their nonvolatility, allowing for significantly higher data retention times compared to dynamic access memory [95, 96], while also possessing significantly faster write times and higher endurance compared to flash [95, 96]. However, two main concerns facing FE random access memory (FeRAM) are they employ FE materials that contain lead, and the readout process is destructive in current implementation [96], requiring a rewrite step in order to prevent the loss of data [96, 97]. Current research interest lies in the fabrication of lead-free ferroelectrics [98, 99, 100], and the implementation of nondestructive readout utilizing optical properties of FE materials, such as the Pockels effect [101, 102]. The Pockels effect is the linear change to the refractive index under the application of an external electrical field. As the change in the refractive index will differ depending on the orientation of the electric dipoles, by measuring the rotation of light passing through the device, the state can be determined nondestructively.

One possible candidate FeRAM device applications is the lead free compound, $BaTiO_3$ (BTO). Recent measurements have shown that thin film BTO crystals grown on unstrained Si have a Pockels coefficient five times higher than LNO, and up to 100 times on strained Si [101]. When doped with $Ba(Cu_{1/3}Nb_{2/3})O_3$ to form (1-x) $BaTiO_3$-$x$$Ba(Cu_{1/3}Nb_{2/3})O_3$ (BT-BCN), x=0.025, its electrial properties, such as its piezoelectric response, are enhanced [99]. In this study, FE BT-BCN structures are grown on Si, with a HfO_2 buffer layer [98]. FE behavior was characterized using domain switching in piezoelectric force microscopy (PFM) measurements and reflectometry measurements were performed in order to measure the index of refraction.

4.3 Samples

Atomic layer deposition was used to grow 10 nm thick HfO_2 layers at 250 ^oC on a p-Si substrate, while BT-BCN was deposited by pulsed laser deposition (PLD) at a temperatures 750-800 ^oC. The BT-BCN target for (PLD) was synthesized using the conventional solid state reaction method and the details can be found in our earlier report [98]. Scanning electron microscopy was performed on two samples providing thicknesses of 90 nm and 600 nm as seen in Fig. 4.2.

4.4 Experimental Details

4.4.1 Piezoelectric Force Microscopy

To demonstrate ferroelectricity in BT-BCN, we have employed PFM (SCM-PIT, Bruker) to probe the local domain configurations and demonstrate switching of the polarization. The PFM topography obtained from the surface of BT-BCN thin film is shown in Fig. 4.1(a). Whereas, Figure 4.1(b) shows the PFM phase micrographs. In these micrographs, polarization is downward at the dark region and polarization is upward where the region is yellow, affirming the 180^o phase difference between two domains [98, 103]. The out-of-plane piezoresponse was recorded as a function of applied voltage. The PFM hysteresis loop in amplitude is shown in Fig. 4.1(c), whereas Fig. 4.1(d) depicts the hysteresis loop in phase. These results establish the ferroelectricity in BT-BCN. In our earlier work, we have also demonstrated the polarization inversion in BT-BCN [98]. It is noteworthy to mention that the presence of domain switching in BT-BCN may be responsible for change in the refractive index [104].

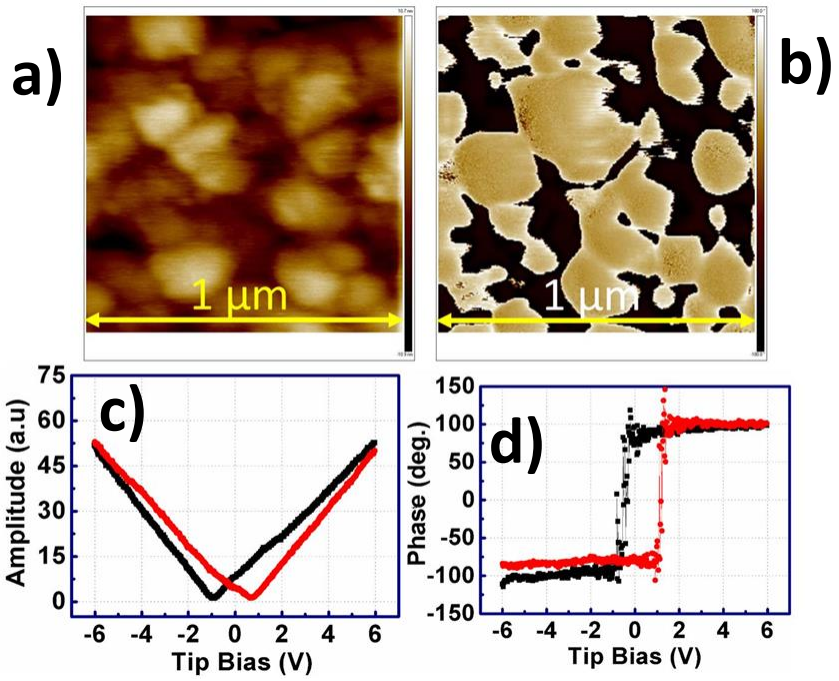

Figure 4.1: a) The PFM topography of 150 nm BT-BCN, and b) PFM phase micrograph. FE behavior can be shown by the hysteresis in the amplitude and phase component of the PFM, as seen in figures c) and d).

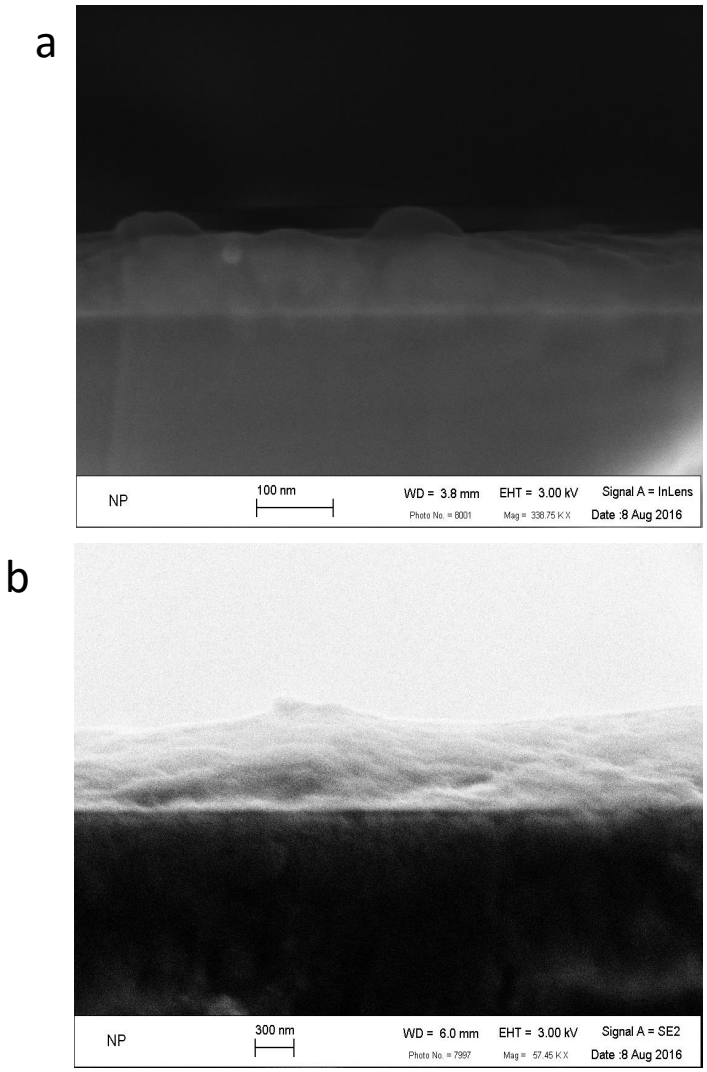

Figure 4.2: SEM measurements for two samples, with a growth temperature of 800 ^{o}C. The thickness of the layer in sample a) is 90 nm, while the average thickness of the sample in b) is 600 nm.

4.4.2 Reflectometry Measurements

Reflectometry measurements were performed in order to measure the index of refraction of BT-BCN. Figure 4.3 shows the schematic of the experimental set up. The polarization of the laser, represented in black, is initially s-polarized, and a Glan Cube is employed in order to change the polarization angle. The light then reflects off the sample, which changes the polarization angle due to the differences in the reflection coefficient between s and p-polarized electric field components. The reflected light passes through an analyzer, before reaching to the detector. In our set up, the light source was a 798 nm Ti:sapphire oscillator, with a pulse duration of 100 fs and a repetition rate of 80 MHz, and intensities of up to 3 μW on the sample, and chopped at a frequency of 331 Hz. The polarization of the reflected light was calculated by varying the analyzer angle, which modulates the intensity as following:

$$I = Acos(\psi - \theta')^2 + B \tag{4.1a}$$

$$I = (A + c\psi)cos(\psi - \theta')^2 + B \tag{4.1b}$$

where we define I as the intensity, A represents the amplitude, B is the background level, ψ and θ' are the analyzer and the reflected polarization angles, respectively. Eq. 4.1(a) is for a perfect analyzer, however, if the light passes through the analyzer off center, then the intensity may be modulated due to imperfections in the analyzer. To correct for this, a first order term was added into the equation. This fact is shown in Eq. 4.1(b), where c represents the first order correction. An example of a fit for finding the reflected polarization angle can be seen in Fig. 4.4(a).

Since the polarization angle can be written as:

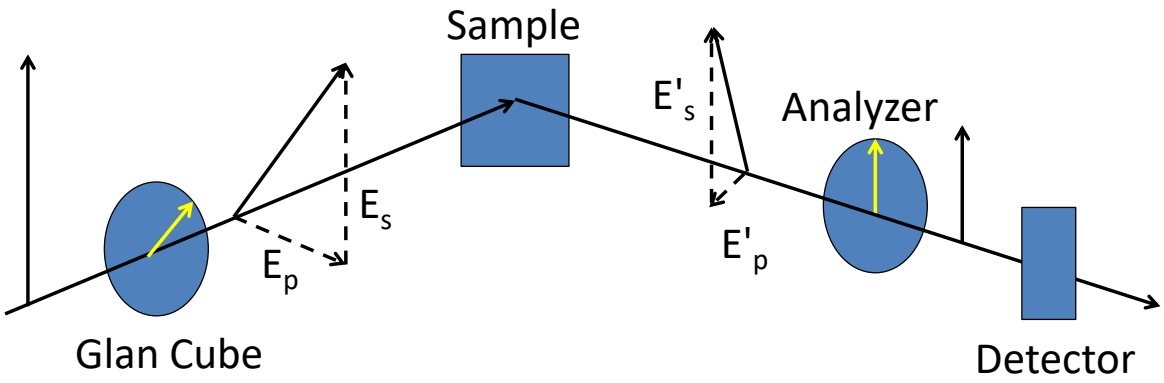

Figure 4.3: A schematic of a reflectometry set up. The s-Polarized light is passed through a Glan Cube, resulting in the transmitted light being at the Glan Cube's angle. When the light reflects off the sample, the p-component of the wave changes by 180^o, and the polarization direction changes due to the differences in the reflection coefficients for s and p-polarized light. The analyzer modulates the intensity reaching to the detector.

$$cot(\theta') = \frac{E'_s}{E'_p} = \frac{r_s E_s}{r_p E_p} = q cot(\theta) \tag{4.2}$$

where θ' (θ) is the polarization direction of the reflected (incident) light, $r_s(r_p)$ is the reflection coefficient for s (p) polarized light, and q being the ratio of the reflection coefficients. Thus, the ratio of the reflection coefficients was extracted by fitting $cot(\theta')$=q$cot(\theta$-m) with m being the shift, we included due to imperfections in the analyzer and slight differences between the zero position of the polarizer and analyzer. An example fit for the ratio of reflection coefficients for GaAs can be seen in Fig. 4.4(b). The index of refraction was extracted by using the Fresnel equation (4.3), where the index of refraction for air was already set to 1, ϕ is the incident angle, and n is the index of refraction, assuming an isotropic sample.

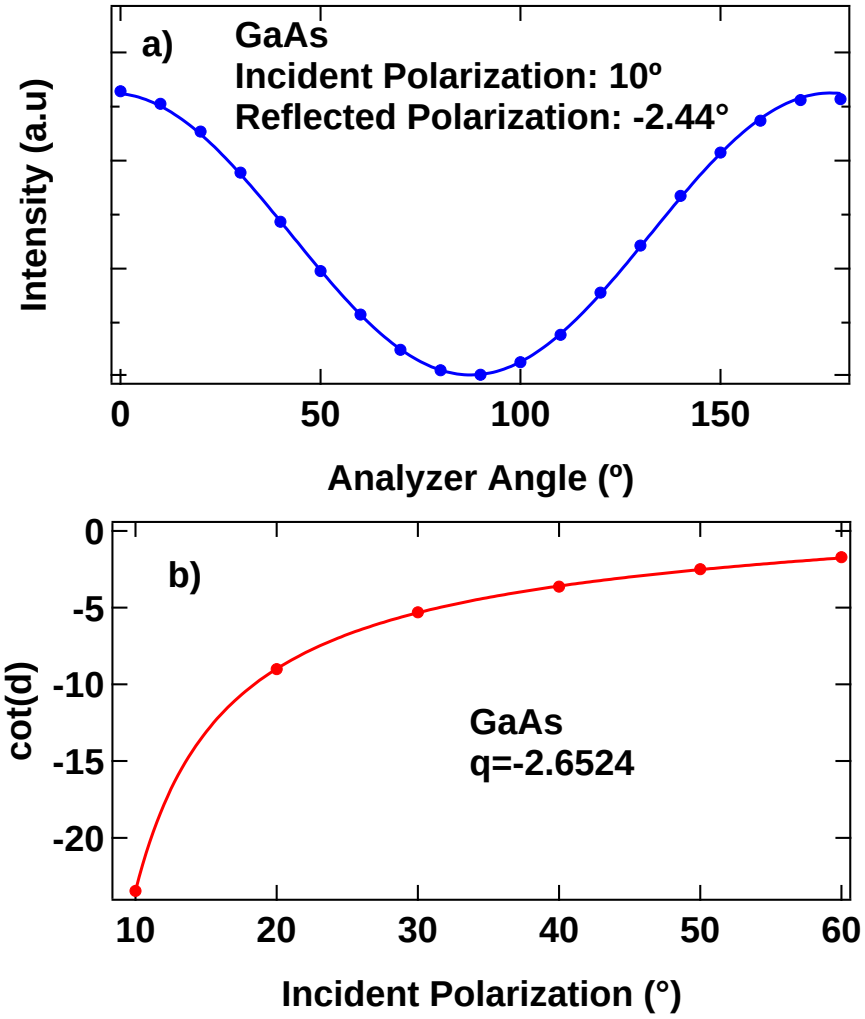

Figure 4.4: a) Light initially polarized at 10^o was reflected off the sample, changing the polarization to -2.44^o. the fitting for the reflected polarization was repeated for different incident polarizations, and the *cot* of the reflected polarization was extracted. Fitting this to the function q$cot(\theta$-$m)$, as seen in b), yields the ratio of the reflection coefficients to be -2.65. Plugging this value back into the Fresnel equations, resulted in the incident angle of 61.5^o.

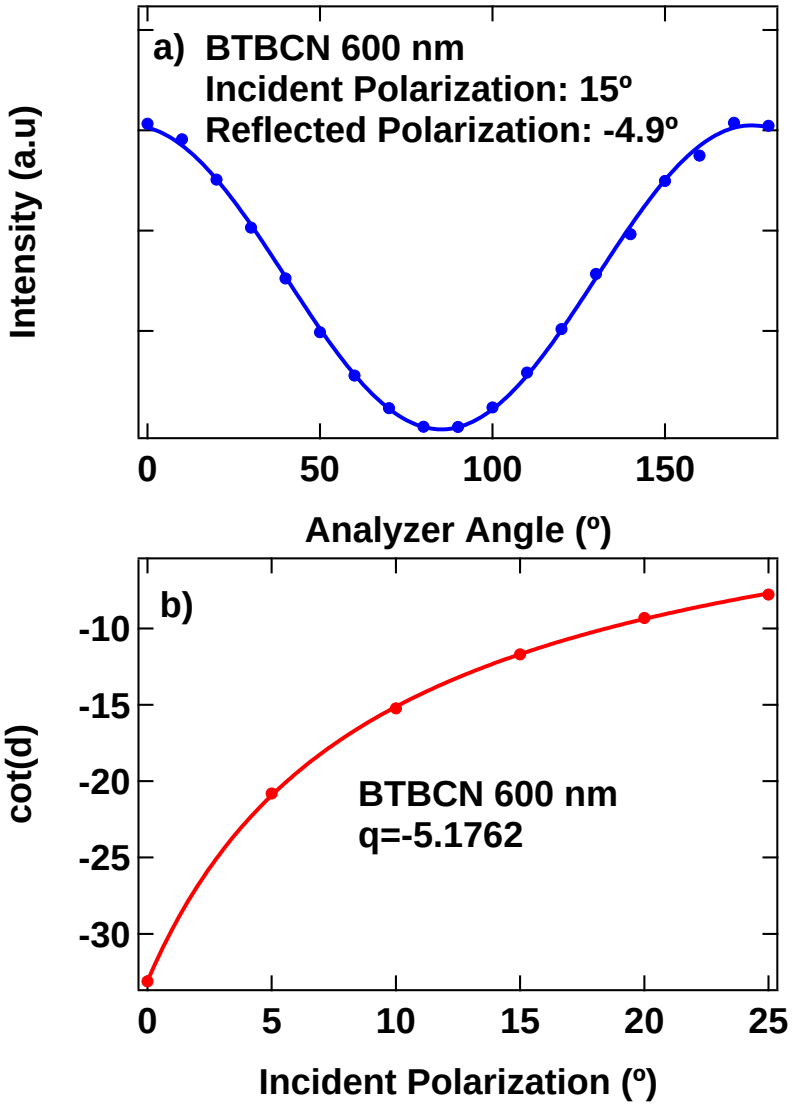

Figure 4.5: a) An example of fitting for the reflected polarization with an incident polarization of 15^o, for the BT-BCN sample grown at 800 ^{o}C. b) Shows a fit for the ratio of reflection coefficients, q. In this case, q=-5.2 on the basis of the GaAs measurements and the angle of incidence was found to be 59.9^o, thus the calculated index of refraction is 2.37.

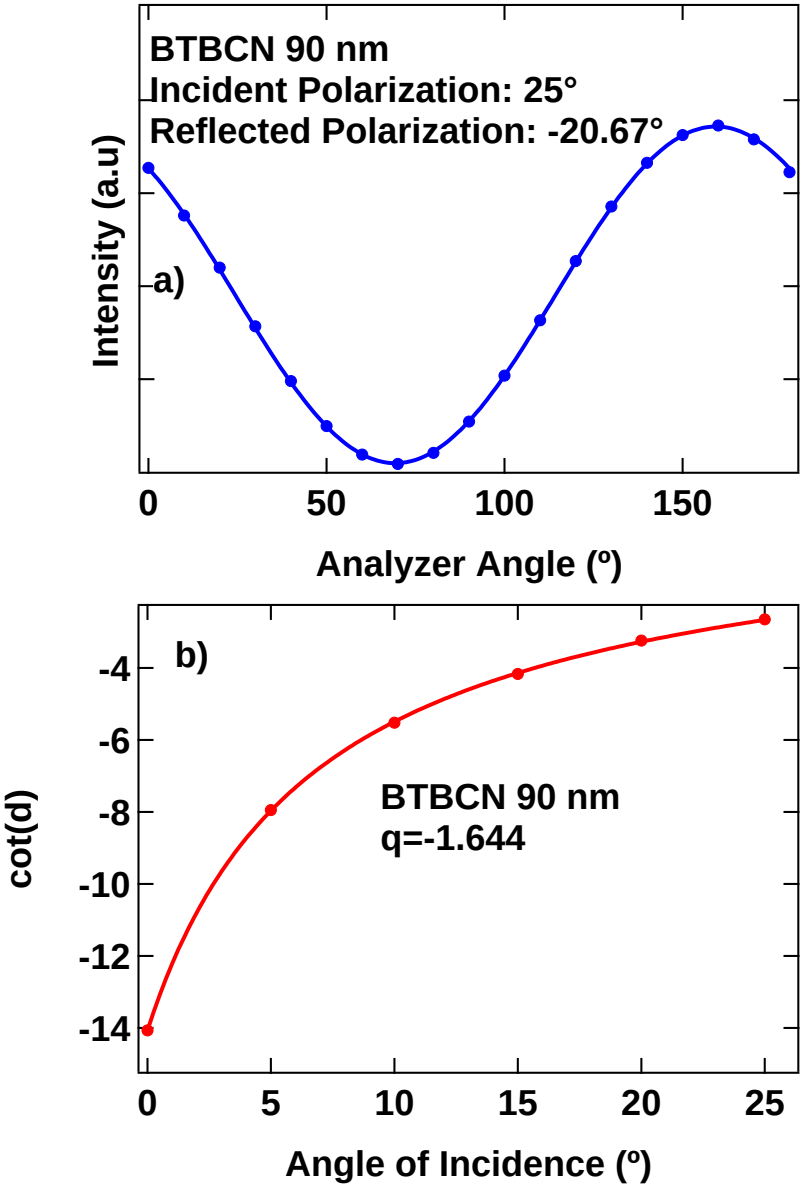

Figure 4.6: a) An example showing the fit for the reflected polarization with an incident polarization of 25^o, for 90 nm BT-BCN. The incident polarization was varied, and the *cot* of the reflected polarization was chosen as a fitting parameter in Eq. 4.2. Panel b) shows the variation of *cot* as a function of the incidence angle, yielding the ratio of the reflection coefficients to be -1.6. The angle of incidence was determined to be 37^0; which corresponds to a refractive index of 1.97.

$$q = \frac{r_s}{r_p} \tag{4.3}$$
$$r_s = \frac{cos(\phi) - \sqrt{n^2 - sin(\phi)^2}}{cos(\phi) + \sqrt{n^2 - sin(\phi)^2}}$$
$$r_p = \frac{n^2 cos(\phi) - \sqrt{n^2 - sin(\phi)^2}}{n^2 cos(\phi) + \sqrt{n^2 - sin(\phi)^2}}$$

In order to determine the incident angle, first the ratio of the reflection coefficients for GaAs was determined. In this process using Eq. 4.3, we were able to calculate the angle of incidence, considering the index of refraction of GaAs to be known and given by [105]. The samples were measured multiple times at a given angle of incidence and were averaged, while the angle of incidence was calculated between 4 and 17 times per sample. An example fit for the 600 nm BT-BCN sample can be seen in Fig. 4.5, whereas examples for the 90 nm and 1.5 nm samples are shown in Fig. 4.6 and Fig. 4.7 , respectively.

Our measurements were performed on BT-BCN with thicknesses of 1.5, 90 and 600 nm. A summary of the average index of refraction for these samples, as well as the statistical errors can be found in Table 4.1. The resulting values of the index of refraction were calculated using Eq. 4.1, where $n(\bar{\theta}_i)$ is the average index calculated at each angle, and i is the number of angles used. The presented error in Table 4.1, is calculated using Eq. 4.2.

$$n = \frac{\sum_i \bar{n}(\phi_i)}{i} \tag{4.1}$$
$$\delta n = \sqrt{\frac{\sum_i (n - \bar{n})^2}{i * (i - 1)}} \tag{4.2}$$

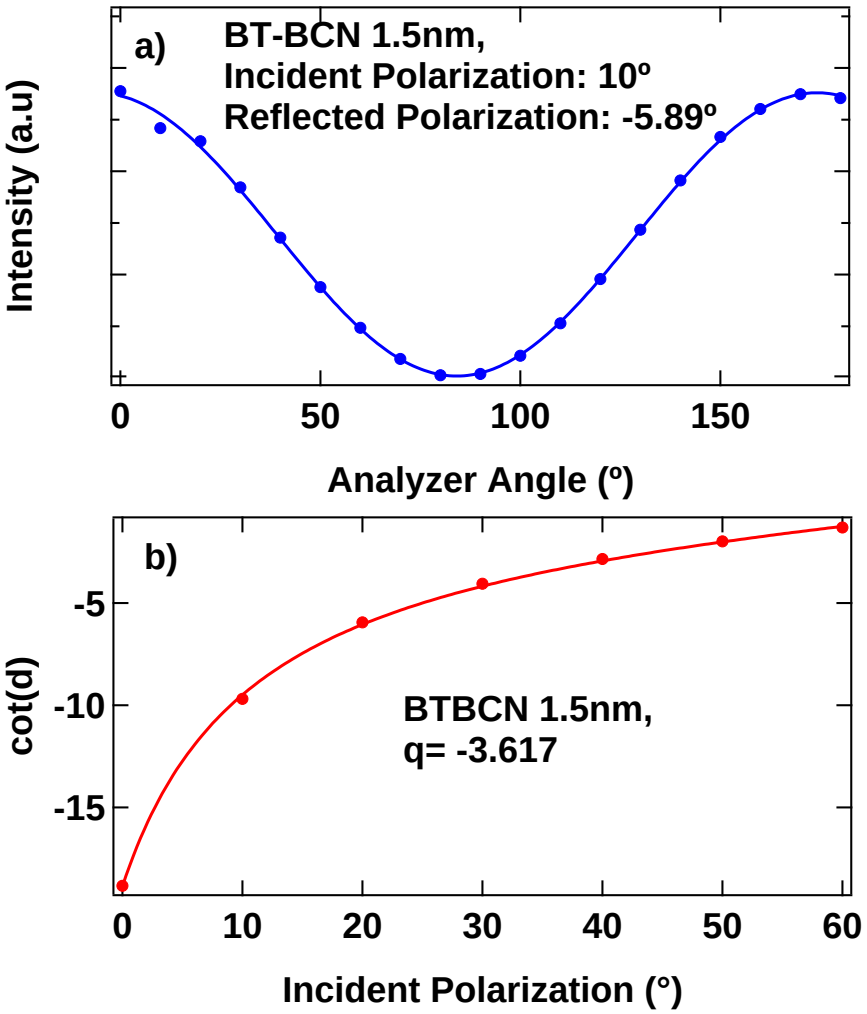

Figure 4.7: a) An example of the fitting for the reflected polarization with an incident polarization of 10^o for the 1.5 nm sample.b) With a ratio of reflection coefficients of -3.617, and an incident angle of 62.4^o fit to 4.2, the refractive index was determined to be 3.12, which is higher than the other two samples.

Table 4.1: The index of refraction, and the errors calculated by the standard deviation for the three samples.

Sample Thickness (nm)	Index of Refraction	Growth T	Structure (^{o}C)	Reference
1.5	2.99 ± 0.03	750	poly x	This Work
90	1.96 ± 0.06	750	poly x	This Work
600	2.32 ± 0.15	800	poly x	This Work
≥1 μm	1.98	27	amorphus	[107]
≥ 1μm	1.95	227	amorphus	[107]
≥ 1μm	2.02	337	micro x	[107]
500	2.03	700	poly x	[108]
	1.8	300	amorphus	[106]
	1.9	650	poly x	[106]
	2.4	750	poly x	[106]
	2.37		x-stal	[109]

4.5 Discussion

As seen in Table 4.1, the index of refraction for the 1.5 nm sample is significantly larger than that of the other samples. A possible explanation for this phenomenon is that there could be some light reaching to the HfO_2 layer, in which the reflected polarization would depend on the reflection coefficients of the BT-BCN layer and the HfO_2 layer. On the other hand, the 90 nm sample has a refractive index that is comparable to that of polycrystalline BTO samples, with a lower growth temperature. Table 4.1 shows a list of refractive indices measured for BTO by different groups, along with the sample structure, at or near 798 nm, either by estimating the values from their figures or using their fits to the Sellmeier equation. In [106] the index of refraction was found to greatly increase by increasing the temperature from 600 to 700 ^{o}C, this fact was attributed to crystallization, while the grain size can increase at higher temperatures leading to a higher index of refraction. Since BT-BCN has a significantly smaller grain size compared to BTO for similar growth conditions [99], this

could be a possible explanation for the lower refractive index of BT-BCN despite the higher growth temperature. As the sample thickness increased to 600 nm, the index of refraction drastically increased to 2.29, which may be related to an increase in grain sizes. Aside from grain size effects, the difference in the electronic structure could potentially contribute to the difference in the refractive index, as the tetragonality of BT-BCN at our BCN concentration is ∼1.007. This concentration compared to BTO with ∼1.01, can enhance the polar nature of the material [99] and the band gap (4.38 eV for BT-BCN [98] compared to 3.75 eV for polycrystalline BTO [106]). Furthermore, [107] concluded that the density difference between crystalline and polycrystalline BTO cannot explain the full difference between their refractive indices.

4.6 Conclusion

Our PFM results have shown that the BT-BCN samples are indeed FE and we are able to switch the polarization directions. The index of refraction obtained for the 1.5 nm thick BT-BCN sample is likely due to a mixture effects from the BT-BCN layer and the HfO_2 layer. The refractive index for the 90 nm thick sample is closer to that of polycrystalline BTO samples with a lower growth temperature. The refractive index of the 600 nm thick samples shows a value much closer to polycrystalline BTO with higher growth temperatures, this fact could be related to an increased grain size.

4.7 Acknowledgment

This work was supported by the AFOSR through grant FA9550-14-1-0376.

Chapter 5

Review and Future Endeavors

5.1 Review

The studies discussed in this dissertation have focused on utilizing optical techniques to characterize novel material systems. These material systems include the ternary alloy InAsP, where pump-probe spectroscopy has gleaned information concerning the carrier and spin relaxation dynamics, the ferromagnetic semiconductors InMnAs and InMnSb, in which my magnetic circular dichroism (MCD) measurements allowed us to determine the spin-orbit split-off (SO) to conduction band (CB) transition; and the lead-free ferroelectric (FE) BT-BCN, with my reflectometry measurements providing the refractive index.

Chapter 2 detailed my pump-probe spectroscopy of InAsP ternary alloys in order to provide insight in the carrier and spin relaxation dynamics. In this study, LO phonon bottlenecking caused an initial delay in the relaxation dynamics. The carrier and spin dynamics of $InAs_xP_{1-x}$ ternary alloys also shows different behaviors for the sample containing x=0.4, and samples containing higher As concentrations. The x=0.4 sample was found to

have carrier and spin relaxation times closer to that of InP, and were found to be an order of magnitude higher than samples with higher As content, which had relaxation times closer to that of InAs. Furthermore, these relaxation times in the x=0.4 sample were found to vary with the excitation wavelengths, allowing for the ability to tune these times depending on the desired device characteristics.

In chapter 3, I discuss my study of the MCD of the ferromagnetic semiconductors InMnAs and InMnSb. The MCD of InMnAs and InMnSb show an oscillatory like behavior which is typically associated with interference effects, however the transmission through the sample shows no evidence of interference and thus the oscillatory behavior is solely due to MCD. The SO to CB transition was identified, and a theoretical model was fit to our experiments in order to determine the sp-d coupling constants. Furthermore, by utilizing the temperature and magnetic field dependence of this transition, we were able to determine the Varshni coefficients for the SO-CB transition, as well as the difference in g-factor between the SO and CB. The Varshni coefficients for the SO-CB transition in InMnSb was found to be similar to theoretical values of InSb.

In chapter 4, I performed reflectometry on BT-BCN in order to determine the refractive indices. The refractive index for the thinnest sample was found to be significantly higher than that of the thicker samples, as well as those of barium titanate (BTO), which may originate from a second order reflection off the HfO_2 buffer layer, or possible intermixing between the BT-BCN and HfO_2. The refractive indices of the thicker samples were found to be similar to that of BTO deposited at a lower temperature than the growth temperature of BT-BCN. This may be related to smaller grain sizes of BT-BCN compared to BTO of the same growth temperature.

5.2 Future Endeavors

The works in this dissertation were typically first steps for studying these novel material systems. In this section, I discuss possible complementary studies which can provide new insight into the physics and engineering of these material systems.

My study of InAsP concerned the carrier and spin relaxation dynamics, which can be manipulated in a variety of manners. One future experiment could involve growing this material as quantum wells, where the interface between the barrier layer and InAsP can be engineered in order to change the surface interface asymmetry. In the Dyakonov-Perel (DP) spin relaxation mechanism, asymmetry of the crystal structure produces an effective magnetic field, and thus a well with a high surface interface asymmetry can result in faster spin relaxation. However, quantum well samples grown in the (110) direction had a suppression of DP spin relaxation, which were previously seen in InAs/GaSb superlattices [49]. Furthermore semiconductor based devices depend on doping the semiconductor material which can introduce impurities, diminishing the effect of DP spin relaxation, previously observed in InAs [47]. However, increased electron-impurity scattering may also decrease the spin relaxation times due to the Elliot-Yafet mechanism, where spin states are not pure due to band mixing and thus scattering has a chance to change the spin. Therefore, the effect of doping on the spin relaxation time is an interesting avenue to be explored. Finally, as this material system can be of interest for photo-detectors for quantum communication applications which depend on the material being in a magnetic field [8], probing magnetic field dependence of the carrier and spin relaxation time is important for this material system.

In chapter 3, I performed magnetic circular dichroism measurements in order to probe the band structure of InMnSb and InMnAs. One possible direction for future study is to perform optically pump nuclear magnetic resonance (OPNMR), which also provides infor-

mation about the band structure. In OPNMR, electrons are excited to the conduction band with through the absorption of circularly polarized light, providing a net electron spin polarization. Due to the interaction between the electrons and ions, the spins of the ions also become polarized, which can be detected through nuclear magnetic resonance. Due to the OPNMR signal being determined by both the sign and magnitude of the spin polarization, it may be possible to resolve contributions from the light hole to conduction band transition [110]. In our MCD study, the high magnetic field lead to a high degree of heavy hole and light hole band mixing, greatly complicating the analysis.

As BT-BCN is a new material system, there are many different studies that can be performed in order to gain insight the properties of this material. As this material is being investigated for potential uses in ferroelectric (FE) memories, the enviroment of the structure can exceed room temperature. As one method of optical reading FE memory state depends on the refractive index, determining the stability of the refractive index with respect to temperature is a great concern. Furthermore, utilization of the Pockels effect for memory applications depends on the orientation of the electric dipole with respect to an external electric field. Aside from the 180 ^{o} FE domains, polycrystalline BT-BCN will have 90^o domains, resulting in a different change of the refractive index than that of the 180^o domains, comparatively decreasing the rotation. Single crystalline BT-BCN material can help solve this issue, however the required growth temperature may damage the substrate and structure. In order to create a single crystal structure, laser annealing can be attempted to selectively heat spots in the BT-BCN layer and this may be performed using the confocal microscope.

Bibliography

[1] . Piskorski, R. P. Sarzaa, and W. Nakawaksi, Opto-Electron. Rev. 19,320 (2011).

[2] D. Elvira, R. Hostein, F. Bruno, L. Monniello, A. Michon, G. Beaudoin,R. Braive, I. Robert-Philip, I. Abram, I. Sagnes, and A. Beveratos, Phys. Rev. B 84 , 195302 (2011).

[3] M. Wada and H. Hosomatsu, Appl. Phys. Lett.64, 1265 (1994).

[4] H. Sugiura, J. Cryst. Growth, 164, 434 (1996).

[5] R. U. Martinelli, T. J. Zamerowksi, and P. A. Longeway, Appl. Phys. Lett. 54, 277 (1989).

[6] M. K. Hudait, Y. Lin, and S. A. Ringel, J. Appl. Phys. 105, 061643 (2009).

[7] H. Kosaka, A. A. Kiselev, F. A. Baran, K. W. Kim, and E. Yablonovitch, Electron. Lett. 37, 464 (2001).

[8] R. Vrijen, and E. Yablonovitch, Physica E 10, 569 (2001)

[9] H. Ohno, Science 281, 951 (1998).

[10] N. Rangaraju, J. A. Peters, and B. W. Wessels, Phys. Rev. Lett. 105, 117202 (2010).

[11] Andrei Kirilyuk, Alexey V. Kimel, and Theo Rasing, Reviews of Modern Physics, 82, 2731 (2010).

[12] Friedman, J.S.; Rangaraju, N.; Ismail, Y.I.; Wessels, B.W., Nanotechnology, IEEE Transactions on Nanotechnology , 11 Issue: 5, 1026 (2012); also Friedman and Wessels Proc. Nanoarch 2012.

[13] B. W. Wessels InMnAs Thin Films and Heterostructures in Handbook of Spintronic Semiconductors, Editors Weimin Chen; Irina Buyanova (Pan-Stanford Publishing 2010).

[14] P. T. Chiu, S. J. May, and B. W. Wessels, Appl. Phys. Lett. 85, 780 (2004).

[15] J. A. Peters and B. W. Wessels, Physica E 42,1447 (2010).

[16] C. E. Feeser, L. Lari, V. K. Lazarov, J. A. Peters, and B. W. Wessels, J. Vac. Sci. Technol. B 30, 032801 (2012).

[17] a) A. J. Blattner, J. Lensch and B. W. Wessels, J. Electron. Mater 30, 1408 (2001).

b) A. J. Blattner and B. W. Wessels, J. Vac. Sci. Technol. B 20, 1582 (2002).

c) A. J. Blattner and B. W. Wessels, Appl. Surface Science 221, 155 (2004).

[18] a) H. Munekata, H. Ohno, S. von Molnar, A. Segmuller, L. L. Chang, and L. Esaki, Phys. Rev. Lett. 63, 1849 (1989).

b) H. Munekata, A. Zaslavsky, P. Fumagalli, R.J. Gambino, Appl. Phys. Lett. 63, 2929 (1993).

[19] H. Ohno, A. Shen , F. Matsukura, A. Oiwa, A. Endo, S. Katsumoto, and Y. Iye, Appl. Phys. Lett. 69, 363 (1996).

[20] J. Inoue, S. Nonoyama, and H. Itoh, Phys.Rev. Lett. 85, 4610 (2000)

[21] J. Schliemann and A. H. MacDonald, Phys. Rev. Lett. 88, 137201 (2002).

[22] A. H. MacDonald, P. Schiffer and N. Samarth, Nature Materials 4, 195 (2005).

[23] Burch, K., Awschalom, D. and Basov, D. Optical properties of III-Mn-V ferromagnetic semiconductors J. Magn. Magn. Mater. 320, 3207 (2008).

[24] M. A. Mayer, P. R. Stone, N. Miller, H. M. Smith, III, O. D. Dubon, E. E. Haller, K. M. Yu, W. Walukiewicz, X. Liu and J. K. Furdyna, Phys. Rev. B 81, 045205 (2010).

[25] S. Salahuddin, and S. Datta, Nano Lett. 8, 405-410 (2008)

[26] J. Müller, P. Polakowski, S. Mueller, and T. Mikolajick, ECS J. Solid State Sci. Technol.4 (5), N30-N35 (2015)

[27] R. Pandey, H. Madan, H. Liu, V. Chobpattana, M. Barth, B. Rajamohanan, M. J. Hollander, T. Clark, K. Wang, J.-H. Kim, D. Gundlach, K. P. Cheung, J. Suehle, R. Engel-Herbert, S. Stemmer, and S. Datta, in Proceedings of the IEEE Conference Symposia on VLSI Technology (2015), p. 206

[28] Y. Zhu, M. K. Hudait, D. K. Mohata, B. Rajamohanan, S. Datta, D. Lubyshev, J. M. Fastenau, and A. K. Liu, J. Vac. Sci. Technol. B 31, 041203 (2013)

[29] R. Q. Yang, B. H. Yang, D. Zhang, C.-H. Lin, S. J. Murry, H. Wu, and S. S. Pei, Appl. Phys. Lett. 71, 2409 (1997).

[30] M. Yamaguchi, T. Takamoto, K. Araki, and N. Ekins-Daukes, Sol. Energy 79, 78 (2005).

[31] J. F. Geisz, D. J. Friedman, J. S. Ward, A. Duda, W. J. Olavarria, T. E. Moriarty, J. T. Kiehl, M. J. Romero, A. G. Norman, and K. M. Jones, Appl. Phys. Lett. 93, 123505 (1991).

[32] I. A. Young, U. E. Avci, and D. H. Morris, in Proceedings of the IEEE Conference of Electron Devices Meeting (IEDM) (2015), p. 600.

[33] J-S. Liu, M. B. Clavel, R. Pandey, S. Datta, M. A. Meeker, G. A. Khodaparast, and M. K. Hudait, J. Appl. Phys. 119, 244308 (2016)

[34] Y. Zhu, N. Jain, S. Vijayaraghavan, D. K. Mohata, S. Datta, D. Lubyshev, J. M. Fastenau, W. K. Liu, N. Monsegue, and M. K. Hudait, J. Appl. Phys. 112, 024306 (2012).

[35] S. Xiaoguang, W. Shuling, J. S. Hsu, R. Sidhu, X. G. Zheng, X. Li, J. C. Campbell, and A. L. Holmes, IEEE J. Sel. Topics Quantum Electron. 8, 817 (2002)

[36] J.R. PESSETTO, and G.B. STRINGFELLOW , J. Cryst. Growth 62, 1-6 (1983)

[37] S. Niu, X. Fang, D. Fang, J. Li, J. Tang, X. Wang, F. Fang, and Z. Wei, Preceedings International Conference on Logistics Engineering, Management and Computer Science (LEMCS 2015), 513-514

[38] N. Terasaki and C. N. Xu, IEEE Sens. J. 13, 3999-4004 (2013)

[39] N. Terasaki, H. Yamada, and C. N. Xu, Catal. Today 201, 203-208 (2013)

[40] C. N. Xu, T. Watanabe, M. Akiyama, and X. G. Zheng, Appl. Phys. Lett. 74, 1236-1238 (1999)

[41] M. K. Hudait, M. Clavel, P. S. Goley, Y. Xie, and J. J. Heremans, Appl. Mater Interfaces 7 (40), 22315-23321 (2015).

[42] H. Kosaka, A.A. Kiselev, F.A. Baron, K.W. Kim, and E. Yablonovitch, Electronics Letters **37**, 464 (2001).

[43] H. Ma, Z. Jin, L. Wang, and Guohong Ma, J. Appl. Phys. **109**, 023105 (2011).

[44] Bo Li, Maria C. Tamargo, Carlos A. Merilesa, App. Phys. Lett. 91, 222114 (2007).

[45] C. P. Weber and Eric A. Kittlaus, J. of Appl. Phys. 113, 053711 (2013).

[46] M. Ikezawa, and B. Pal, Y. Masumoto, I. V. Ignatiev, S. Yu Verbin, and Il'ya Ya Gerlovin, Phys. Rev. B, **72**, 153302 (2005).

[47] P. Murzyn, C. R. Pidgeon, P. J. Phillips M. Merrick, K. L. Litvinenko, J. Allam, B. N. Murdin, T. Ashley and J. H. Jefferson, L. F. Cohen, Appl. Phys. Lett., **83**, 5220 (2003).

[48] T. F. Boggess, J. T. Olesberg, C. Yu, M. E. Flatte, and W. H. Lau, Appl. Phys. Lett, **77**, 1333 (2000).

[49] K. C. Hall, K. Gündogdu, E. Altunkaya, W. H. Lau, M. E. Flatté, and Thomas F. Boggess, J. J. Zinck, W. B. Barvosa-Carter, and S. L. Skeith, Phys. Rev. B. **68**, 115311 (2003).

[50] K. L. Litvinenko, B. N. Murdin, J. Allam, Tong Zhang, J. J. Harris, and L. F. Cohen, D. A. Eustace and D. W. McComb, Phys. Rev. B **74**, 075331 (2006).

[51] R. N. Kini, K. Nontapot, G. A. Khodaparast, R. E. Welser, and L. J. Guido, J. Appl. Phys. **103** , 064318 (2008).

[52] S. G. Choi, C. J. Palmstrøm, Y. D. Kim, D. E. Aspnes, H. J. Kim, and Y. C. Chang, Appl. Phys. Lett **91**, 041917 (2007).

[53] J. Nunnenkamp, J. H. Collet, J. Klebniczki, J. Kuhl, K. Ploog, Phys. Rev. B, **43**, 14047 (1991).

[54] R. J. Elliot, Phys. Rev. 96, 266 (1954).

[55] M. I. Dyakonov and V. I. Perel, Zh. Eksp. Teor. Fiz. 60, 1954 (1971) [Sov. Phys. JETP 33, 1053 (1971)]; Fiz. Tverd. Tela (Leningrad) 13, 3581 (1971) [Sov. Phys. Solid State 13, 3023 (1972)].

[56] Y. Ohno, R. Terauchi, T. Adachi, F. Matsukura, and H. Ohno, Phys. Rev. Lett. 83, 4196 (1999).

[57] T. Wojtowicz, G. Cywinski, W. L. Lim, X. Liu, M. Dobrowolska, J. K. Furdyna, K. M. Yu, W. Walukiewicz, G. B. Kim, M. Cheon, X. Chen, S. M. Wang, and H. Luo, Appl. Phys. Lett. **82**, 4310 (2003).

[58] T. Wojtowicz, W. L. Lim, X. Liu, G. Cywinski,M. Kutrowski, L. V. Titova, K. Yee, M. Dobrowolska, J. K. Furdyna, K. M. Yu, W. Walukiewicz, G. B. Kim, M. Cheon, X. Chen, S. M. Wang, H. Luo, I. Vurgaftman, J. R. Meyer, Physica E **20**, 325 (2004).

[59] M. Tanaka, S. Ohya, and P. N. Hai, App. Phys. Rev. **1**, 011102 (2014).

[60] M. Tanaka and S. Ohya, Spintronic devices based on semiconductors in Comprehensive Semiconductor Science and Technology, edited by P. Bhattacharya, R. Fornari, and H. Kamimura (Elsevier, Amsterdam, 2011), Vol. 6, pp. 540-562.

[61] H. Ohno, A. Shen, F. Matsukura, A. Oiwa, A. Endo, S. Katsumoto, and H. Iye, Appl. Phys. Lett. **69**, 363 (1996).

[62] G. A. Khodaparast, R. E. Doezema, S. Chung, K. Goldammer, and M. B. Santos, Phys. Rev. B **70**, 155322 (2004).

[63] M. Frazier,J. G. Cates,J. A. Waugh,J. J. Heremans,M. B. Santos,X. Liu,and G. A. Khodaparast, J. of Appl. Phys. **106**, 103513 (2009).

[64] O. Olendski, Q. L. Williams, and T. V Shahbazyan, Phys. Rev. B **77**, 125338 (2008).

[65] M. Bhowmick, T. Merritt, G. A. Khodaparast, B. W. Wessele, S. A. McGill, D. Saha, X. Pan, G. D. Sanders, and C. Stanton, Phys. Rev. B **85**, 125313 (2012).

[66] H. Munekata, H. Ohno, S. von Molnar, A. Segmuller, L. L. Chang, and L. Esaki, Phys. Rev. Lett. **63**, 1849 (1989).

[67] H. Ohno, H. Munekata, S. von Molnar, and L. L. Chang, J. Appl. Phys. **69**, 6103 (1991).

[68] A. J. Blattner and B. W. Wessels, Appl. Surf. Science, **221**,155 (2004).

[69] N. Rangaraju, Li Pengcheng, and B. W. Wessels, Phys. Rev. B **79**, 205209 (2009).

[70] N. D. Parashar, N. Rangaraju, V. K. Lazarov, S. Xie, and B.W. Wessels Phys. Rev. B **81**, 115321 (2010).

[71] P. T. Chiu and B. W. Wessels, Appl. Phys. Lett. **89**, 102505 (2006).

[72] P. T. Chiu and B. W. Wessels, Phys. Rev. B, **76**,165201 (2007).

[73] G. A. Khodaparast,Y. H. Matsuda, D. Saha, G. D. Sanders, C. J. Stanton, H. Saito, S. Takeyama, T. R. Merritt, C. Feeser, B. W. Wessels, X. Liu and J. Furdyna, Phys. Rev. B **88**, 235204 (2013).

[74] M. Wang, R. A. Marshall, K. W. Edmonds, A. W. Rushforth, R. P. Campion, and B. L. Gallagher, Appl. Phys. Lett. **104**, 132406 (2014).

[75] A. Winter, H. Pascher, H. Krenn, T. Wojtowicz, X. Liu and J. K. Furdyna, AIP Proc. **893**, 1223 (2007).

[76] A. Winter, H. Pascher, M. Hofmayer, H. Krenn, T. Wojtowicz, X. Liu and J. Furdyna, Adv. Mat. Sci. **20**, 92 (2009).

[77] C. Thurn, V. M. Axt, A. Winter, H. Pascher, H. Krenn, X. Liu, J. K. Furdyna, T. Wojtowicz, Phys. Rev. B **80**, 195210 (2009).

[78] T. Schallenberg and H. Munekata, Appl. Phys. Lett. **89**, 042507(2006).

[79] A.J. Blattner, P.L. Prabhumirashi, V.P. Dravid, B.W. Wessels, J. Cryst. Growth. **259**, 8 (2003).

[80] Y. L. Soo, S. Kim, Y. H. Kao, A. J. Blattner, B. W. Wessels, S. Khalid, C. Sanchez Hanke, and C.-C. Kao, Appl. Phys. Lett. **84**, 481 (2004).

[81] Leonardo Lari, Stephen Lea, Caitlin Feeser, Bruce W. Wessels, and Vlado K. Lazarov, J. of Appl. Phys. **111**, 07C311 (2012).

[82] Caitlin E. Feeser, Leonardo Lari, Vlado K. Lazarov, John A. Peters, and Bruce W. Wessels, J. of Vacuum Science-Technology B **30**, 032801 (2012).

[83] I. Vurgaftman, J. R. Meyer, and L. R. Ram-Mohan. J. Appl. Phys. **89**, 5815 (2001).

[84] M. Dobrowolska, K. Tivakornsasithorn, X. Liu, J. K. Furdyna, M. Berciu, K. M. Yu and W. Walukiewicz, Nature Materials , **11** , 444 (2012).

[85] C. Thurn, V. M. Axt, A. Winter, H. Pascher, H. Krenn, X. Liu, J. K. Furdyna and T. Wojtowicz, Phys. Rev. B **80**, 195210 (2009)

[86] C. K. Pidgeon and R. N. Brown, Phys. Rev. **146**, 575 (1966).

[87] G. D. Sanders, Y. Sun, C. J. Stanton, G. A. Khodaparast, J. Kono, Y. H. Matsuda, N. Miura, T. Slupinski, A. Oiwa, and H. Munekata, J. Appl. Phys. **93**, 6897 (2003).

[88] G. D. Sanders, Y. Sun, C. J. Stanton, G. A. Khodaparast, J. Kono, Y. H. Matsuda, N. Miura, T. Slupinski, A. Oiwa, and H. Munekata, Journal of superconductivity **16**, 449 (2003).

[89] G. D. Sanders, Y. Sun, C. J. Stanton, G. A. Khodaparast, J. Kono, D. S. King, Y. H. Matsuda, S. Ikeda, N. Miura, A. Oiwa, et al., Physica E **20**, 378 (2004).

[90] Y. Sun, F. V. Kyrychenko, G. D. Sanders, C. J. Stanton, G. A. Khodaparast, J. Kono, Y. H. Matsuda, H. Munekata, SPIN **5**, 1550002 (2015).

[91] J. Kossut, Semiconductors and Semimetals **25**, 183 (1988).

[92] M. A. Zudov, J. Kono, Y. H. Matsuda, T. Ikaida, N. Miura, H. Munekata, G. D. Sanders, Y. Sun, and C. J. Stanton, Phys. Rev. B **66**, 161307(R) (2002).

[93] G. A. Khodaparast, J. Kono, Y. H. Matsuda, S. Ikeda, N. Miura, Y. J. Wang, T. Slupinski, A. Oiwa, H. Munekata, Y. Sun, F. V. Kyrychenko, G. D. Sanders, and C. J. Stanton, Physica E **21**, 978 (2004).

[94] B. Beschoten, P. A. Crowell, I. Malajovich, D. D. Awschalom, F. Matsukura, A. Shen and H. Ohno, Phys. Rev. Lett, **83**, 3073.

[95] A. Chanthbouala, A. Crassous, V. Garcia, K. Bouzehouane, S. Fusil, X. Moya, J. Allibe, B. Dlubak, J. Grollier, S. Xavier, C. Deranlot, A. Moshar, R. Proksch, N. Mathur, M. Bibes, and A. Barthélémy, Nat. Nanotech. 7, 101-104 (2012)

[96] R. Guo, L. You, Y. Zhou, Z. S. Lim, X. Zou, L. Chen, R. Ramesh, and J. Wang, Nat. Comm. 4, 1990 (2013) V. Kalinin, A. A. Demkov, and V. Narayanan, Nat. Nanotechnol. 8, 748754 (2013)

[97] P. B. Xiao, W. Zhang, T. L. Qu, Y. Huang, and S. M. Hu,, Chin. Phys. Lett 32, (2015)

[98] S. Kundu, D. Maurya, M. Clavel, Y. Zhou, N. N. Halder, M. K. Hudait, P. Banerji, and S. Priya, Sci. Rep. 5, 8494 (2015)

[99] D. Maurya, A. Kumar, V. Petkov, J. E. Mahaney, R. S. Katiyar, and S. Priya, RSC Adv. 4, 1283 (2014)

[100] D. Maurya, N. Wongdamnern, R. Yimnirun, and S. Priya, J. Appl. Phys. 180, 124111 (2010).

[101] S. Abel, T. Stöferle, C. Marchiori, C. Rossel, M. D. Rossel, R. Erni, D. Caimi, M. Sousa, A. Chelnokov, B. J. Offrein, and J. Fompeyrine, Nat. Commun.4, 1671 (2013)

[102] S. Abel, D. Caimi, M. Sousa, T. Stöferle, C. Rossel, C. Marchiori, A. Chelnokov, and J. Fompeyrine, Proc SPIE 8263, 82630Y-1 (2012)

[103] W. J. Hu, D. M. Juo, L. You, J. Wang, Y. C. Chen, Y. H, Chu, and T. Wu, Sci. Rep. 4, 4772 (2014)

[104] M. J. Dicken, L. A. Sweatlock, D. Pacifici, H. J. Lezec, K. Bhattacharya, and H. A. Atwater, Nano Letters, 8, 4048 (2008)

[105] G. E. Jellison Jr., Opt. Mat. 1, 151-160 (1992)

[106] R. Thomas, D. C. Dube, M. N. Kamalasanan, and S. Chandra, Thin Solid Films 346, 212-225 (1999)

[107] M. Wöhlecke, V. Marrello, and A. Onton, J. Appl. Phys 48, 1748 (1977)

[108] P. C. Joshi, and S. B. Desu, Thin Solid Films 300, 289-294 (1997)

[109] A. R. Johnston, J. App. Phys. 42, 3501 (1971)

[110] K. Ramaswamy, S. Mui, S. A. Crooker, X. Pan, G. D. Sanders, C. J. Stanton, and S. E. Hayes, Phys. Rev. B 82, 085209 (2010).